nature communications

Article

https://doi.org/10.1038/s41467-026-79311-0

Chromosomally unstable cancer cells exhibit heightened dependence on the mitotic SKA complex

Received: 20 April 2026

Accepted: 9 October 2026

Published online: 18 November 2026

Check for updates

Maud Schoot Uiterkamp[1,2], Elsa S. Coolen[1,2,9], Klaas de Lint[3,9], Adi Tarrab[4,9], Kruno Vukušić[5,9], Davy Rockx[3], Martin A. Rooimans[3], Tess de Kleijn[1,2,8], Iris J. Harmsen[6], Rodrigo Leite de Oliveira[3], Floris Foijer[6,7], René H. Medema[1,2], Iva M. Tolić[5], Uri Ben-David[4], Rob M. F. Wolthuis[3] & Gerben Vader[1,2]

Aneuploidy and chromosomal instability are common characteristics of cancer but remain underexploited therapeutically. Chromosomally unstable cells are often selectively vulnerable to inhibition of the kinesin KIF18A, and this dependence is related to altered mitotic control. Here, we identify the spindle and kinetochore-associated (SKA) complex as a mitotic regulator that establishes a similar dependency. SKA complex loss is tolerated in cells with a defective mitotic checkpoint, but when mitosis is prolonged, it leads to mitotic errors and loss of viability. Genetic analysis reveals that the SKA complex and KIF18A are epistatic, although they function through mechanistically distinct mitotic pathways. SKA complex depletion selectively impacts chromosomally unstable cancer cells and mirrors the effects of KIF18A inhibition. We thus identify a cellular vulnerability associated with prolonged mitosis in chromosomally unstable cancers.

Hundreds of proteins coordinate chromosome segregation, rendering them essential for cellular survival (e.g., refs. 1–4). In many cases, this essentiality reflects an inherent requirement for stable genome propagation. Alternatively, lethality associated with protein loss could arise primarily from activation of the spindle assembly checkpoint (SAC), leading to prolonged mitotic arrest and cell death. The SAC, or mitotic checkpoint, senses chromosome segregation defects and halts cell cycle progression by counteracting the E3 ubiquitin ligase anaphase-promoting complex/cyclosome (APC/C) (Supplementary Fig. S1A)[5–7]. The balance between the antagonizing activities of the SAC and APC/C can therefore impact how cells respond to chromosome segregation defects. For example, inhibition or loss of the mitotic kinesin *KIF18A* activates the SAC and can lead to cell death, whereas cells lacking a functional SAC are resistant to KIF18A inhibition (i.e., *KIF18A* is 'synthetic viable' in SAC-deficient conditions)[7,8]. Many chromosomally unstable cancers have rewired control of mitosis[5–8]. Although this may be expected to weaken mitotic checkpoint stringency, in practice these cells often spend longer in mitosis, in a SAC-dependent manner. This characteristic, together with imbalanced and increased chromosome numbers present in these cells, is a major determinant of KIF18A dependency[8–11]. Based on this rationale, small-molecule inhibitors of

[1]Princess Máxima Center for Pediatric Oncology, Utrecht, The Netherlands. [2]Oncode Institute, Utrecht, The Netherlands. [3]Oncogenetics & Oncogenomics, Cancer Center Amsterdam, Department of Human Genetics, Amsterdam University Medical Center, Amsterdam, The Netherlands. [4]Department of Human Genetics and Computational Medicine, Gray Faculty of Medical & Health Sciences, Tel Aviv University, Tel Aviv, Israel. [5]Division of Molecular Biology, Ruđer Bošković Institute, Zagreb, Croatia. [6]European Research Institute for the Biology of Ageing (ERIBA), University of Groningen, University Medical Center Groningen, Groningen, The Netherlands. [7]IPSomics, Groningen, The Netherlands. [8]Present address: Department of Clinical Sciences, Faculty of Veterinary Medicine, Utrecht University, Utrecht, The Netherlands. [9]These authors contributed equally: Elsa S. Coolen, Klaas de Lint, Adi Tarrab, Kruno Vukušić. e-mail: g.vader-2@prinsesmaximacentrum.nl

KIF18A are in phase 1/2 clinical trials to treat genomically highly unstable cancers[12–16].

Results

Genetic identification of SAC-contingent mitotic factors

Given the connection between SAC function and efficacy of KIF18A inhibitors, we reasoned that mapping factors whose essentiality is equally contingent on SAC function may lead to the identification of novel mitotic vulnerabilities with specificity for chromosomally unstable cancers. To pursue this goal, we sought to create human cells that undergo mitosis without a functional SAC. The AAA + ATPase TRIP13 is a key component of SAC signaling[17–19]. TRIP13 catalyzes the conformational conversion of 'closed' MAD2 (c-MAD2) to 'open' MAD2 (o-MAD2), thereby replenishing the o-MAD2 pool required for mitotic checkpoint complex (MCC) formation and SAC function (Supplementary Fig. S1A)[17–34]. *TRIP13* inactivation in near-diploid RPE1-Δ*TP53* cells (hereafter Δ*TRIP13*) altered the levels of MAD2 and the TRIP13-adapter P31^{COMET}[33–35] (Supplementary Fig. S1B). As expected, Δ*TRIP13* cells were unable to mount a SAC-dependent mitotic arrest after treatment with the microtubule drug nocodazole[33–35] (Fig. 1A and Supplementary Fig. S1C). Both phenotypes were reversed upon re-expression of *TRIP13* (Fig. 1A and Supplementary Fig. S1B, S1C). Despite defective checkpoint signaling, Δ*TRIP13* cells remained sensitive to *MAD2L1* loss (Supplementary Fig. S1D, S1E), indicating that the ability to form an initial pool of MAD2-driven MCC remains essential[18,33,34]. No growth defect was observed in Δ*TRIP13* cells, and live-cell imaging did not reveal major defects in mitotic timing, chromosome alignment, or segregation fidelity (Supplementary Fig. S1F, Supplementary Movie 1, 2, Supplementary Fig. S1G). Consistently, *TRIP13* loss did not lead to significant karyotype alterations (Fig. 1B and Supplementary Fig. S1H). Thus, although Δ*TRIP13* cells fail to elicit a prolonged SAC response, cell division is otherwise indistinguishable from that in wild-type cells.

To comprehensively identify factors whose essentiality is impacted by SAC functionality, we performed a genome-wide CRISPR-Cas9 knockout screen in Δ*TRIP13* cells (Supplementary Fig. S2A). This identified two classes of genetic interactions. In one class, genes became more essential when *TRIP13* was absent ('synthetic lethality' (SL)). In the other, genes became less essential in Δ*TRIP13* cells ('synthetic viability' (SV)). We identified 74 SL and 46 SV genes (Fig. 1C and Supplementary Data 1A–C). The APC/C subunit APC15 (encoded by *ANAPC15*) scored as a strong SL hit, validating the screen (Fig. 1C)[18]. Indeed, combined loss of *TRIP13* and *ANAPC15* triggered a mitotic (metaphase) arrest, attributed to an inability to disassemble the MCC[18,36–38], resulting in viability loss (Supplementary Fig. S2B–E).

Inspired by the reported synthetic viable interaction between KIF18A and the mitotic checkpoint[7], we focused our attention on the identified SV genes. Gene ontology (GO) term enrichment analysis of the 46 SV genes revealed significant enrichment for factors involved in mitotic spindle dynamics and chromosome segregation (Supplementary Fig. S2F). Gene Effect Scores for these SV genes (*i.e.*, 'essentiality' scores), derived from the DepMap initiative[39], skewed towards values typical of genes that are classified as 'common essential' (Supplementary Fig. S2G). Taken together, these data hint that these SV genes become essential mainly because their loss triggers a checkpoint-dependent mitotic arrest.

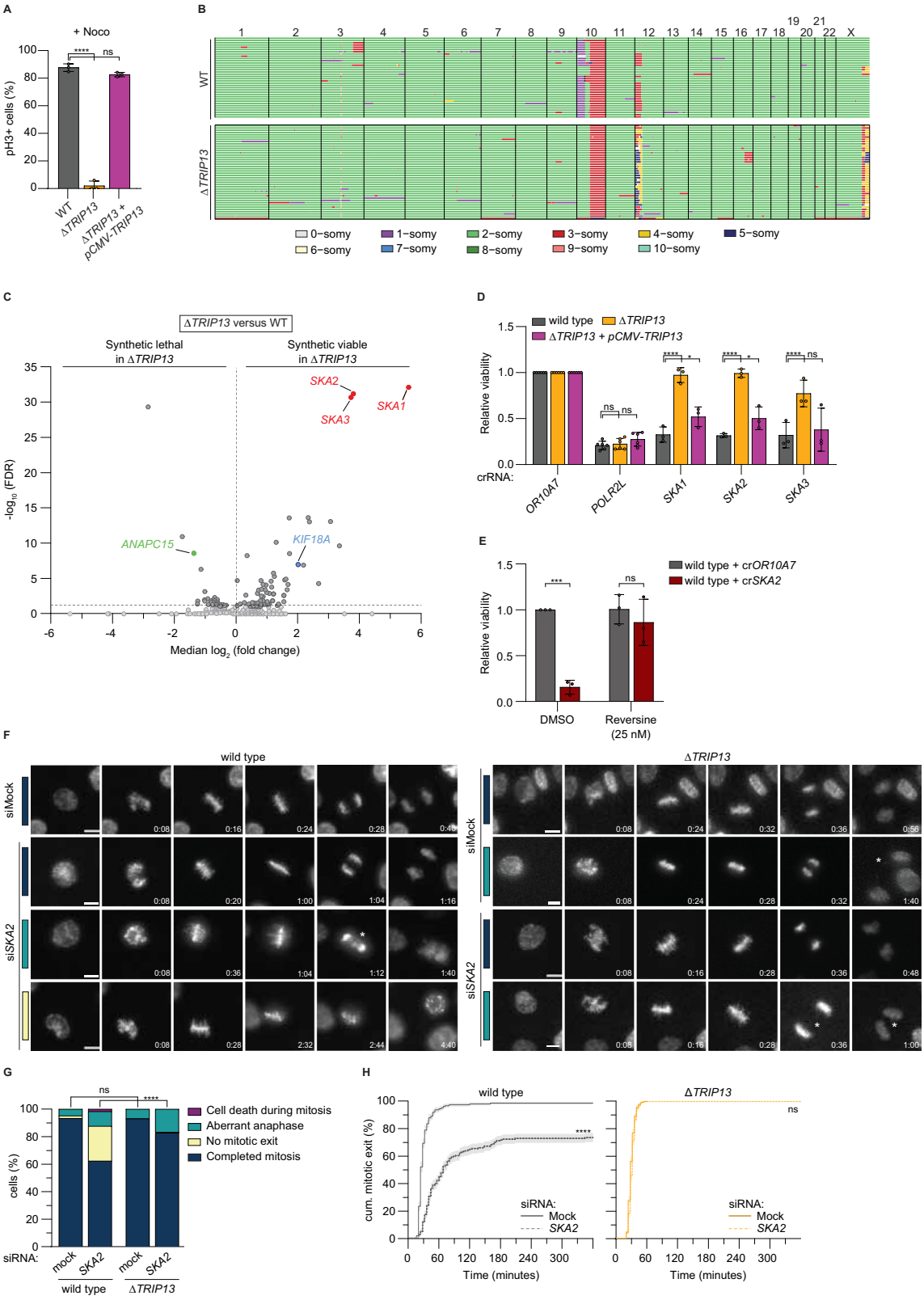
Essentiality of the SKA complex in mitosis is determined by the mitotic checkpoint

Notably, the top SV hits encode all subunits of the spindle and kinetochore-associated (SKA) complex (SKAc): *SKA1, SKA2*, and *SKA3* (Fig. 1C). This trimeric complex stabilizes kinetochore-microtubule attachments and is essential for anaphase onset and mitotic exit[40–54]. Two explanations could account for the observed SV behavior: i) disruption of the identified gene could cause viability loss in wild-type cells, which is suppressed in Δ*TRIP13* cells, or ii) gene disruption could rescue a proliferation defect present in Δ*TRIP13* cells. Analysis of SKAc gRNA abundance demonstrated behavior that is compatible with the former scenario (Supplementary Fig. S2H). Viability and clonogenic assays validated SV behavior upon *SKA1*, *SKA2*, or *SKA3* loss (Fig. 1D and Supplementary Fig. S2I). By using the small-molecule inhibitor Reversine against the essential SAC component MPS1[55] (Supplementary Fig. S1A), we confirmed that synthetic viability of the SKAc in Δ*TRIP13* cells was driven by broad SAC dysfunction (Fig. 1E and Supplementary Fig. S2J). Our screen thus identified a selected list of mitotic factors, prominently among them *SKA1-3*, whose viability defects are mitigated by SAC loss.

We tracked the first mitosis after siRNA-mediated knockdown of *SKA2* by live-cell imaging (experimental set-up in Supplementary Fig. S3A, S3B). In wild-type cells, *SKA2* knockdown markedly increased the fraction of cells that experienced a prolonged mitotic arrest (Fig. 1F, G, Supplementary Fig. S3C and Supplementary Movies 3–6), and doubled mitotic duration from 30 ± 1 to 65 ± 4 min (mean ± SEM, Fig. 1H, Supplementary Fig. S3D), consistent with prior reports[40–44,56,57]. The fraction of aberrant anaphases increased from 5% to 11%, and chromosome alignment was delayed (Fig. 1F, G, Supplementary Fig. S3C, S3E). Conversely, *SKA2* depletion did not induce a metaphase delay in Δ*TRIP13* cells (Fig. 1F–H, Supplementary Fig. S3C and Supplementary Movies 7–10). Instead, these cells progressed through mitosis unimpeded within 31 ± 1 minutes (mean ± SEM) (Supplementary Fig. S3D). Overall, these results demonstrate that loss of TRIP13 circumvents the metaphase delay induced by *SKA2* depletion, explaining the synthetic viability observed in Δ*TRIP13* cells. We also created stable *SKA1, SKA2*, or *SKA3* knockouts in the Δ*TRIP13* background. Consistent with prior studies, loss of any of the three SKA subunits destabilized the entire SKA complex (Supplementary Fig. S3F)[40,41]. Re-expression of *TRIP13* resulted in a near-complete loss of viability in these cells (Supplementary Fig. S3G), indicating that no compensatory, adaptive mechanisms were selected. Mitotic phenotyping of these double knockouts revealed that approximately 86% of all cells progressed through mitosis efficiently; 12% of cells underwent aberrant anaphase compared to 3% of wild-type or Δ*TRIP13* cells (Supplementary Fig. S4A, S4B and Supplementary Movies 11–16). Time to metaphase alignment and total mitotic duration remained similar, with a mitotic duration of 32 ± 1 min in Δ*TRIP13*, 34 ± 1 min in Δ*SKA2*Δ*TRIP13*, and 36 ± 1 min in Δ*SKA3*Δ*TRIP13* cells (mean ± SEM, Supplementary Fig. S4C–E). Consistent with efficient and robust mitotic progression, chromosome counts of Δ*SKA2*Δ*TRIP13* cells were not significantly different from that of either wild-type or Δ*TRIP13* cells, with a mean chromosome number per cell of 45.8 ± 0.1 in wild-type cells, 46.5 ± 1.5 in Δ*TRIP13*, and 45.3 ± 1.5 in Δ*SKA2*Δ*TRIP13* (mean ± SEM, Supplementary Fig. S1H). In line with the notion that a majority of Δ*TRIP13* cells without the SKAc undergo relatively normal mitosis, genome-wide single-cell copy number profiling of Δ*SKA1*Δ*TRIP13*, Δ*SKA2*Δ*TRIP13* and Δ*SKA3*Δ*TRIP13* furthermore revealed a low incidence of aneuploidy (Supplementary Fig. S5). These findings indicate that SKAc loss impacts viability by causing an extended mitotic delay in cells with an intact mitotic checkpoint.

Like the SKAc, *KIF18A* emerged as an SV interactor of *TRIP13* (Fig. 1C), as expected based on earlier reports[7]. Indeed, Δ*TRIP13* cells were less sensitive to *KIF18A* knockout or chemical inhibition using Sovilnesib as compared to wild-type cells[58] (Supplementary Fig. S6A). In addition to *SKA1-3* and *KIF18A*, our screen identified several additional mitotic regulators. These included multiple subunits of the Augmin complex, which promotes microtubule-dependent microtubule nucleation[59–66], as well as the protein kinase *CSNK1A1*, the E3 ligase subunit *CUL3*, the spliceosome component *MAGOH*, and the phosphatase complex *PPP1CB-PPP1R12A* (Fig. 2A and Supplementary Data 1B)[67–73]. All showed SAC-dependent effects on viability (Supplementary Fig. S6B–E). In contrast, core mitotic regulators such as *PLK1*, *AURKA*, *NDC80* and *NUF2* remained essential regardless of *TRIP13*

https://doi.org/10.1038/s41467-026-79311-0



status (Supplementary Fig. S6F). Thus, our SV hits form a unique subset of mitotic regulators defined by SAC-contingent essentiality.

Genetic co-dependence between KIF18A and SV factors

To explore whether the genetic parallels between *KIF18A* and SV factors observed in SAC-deficient RPE1 cells can be extrapolated to other (SAC-proficient) cellular contexts, we analyzed CRISPR-mediated loss-of-function effects in a large cohort of human cancer cell lines, available from the DepMap initiative[39]. Comparing the impact on cellular survival of loss of SV factors to that of KIF18A interestingly revealed significant genetic similarities (*i.e.*, co-dependence) between *KIF18A* and *SKA1, SKA3, HAUS1-8, CSNK1A1* and *PPP1R12A* across a wide range of cancer cell lines (Fig. 2B and Supplementary Data 2A). We note that *SKA1* exhibited the second highest *KIF18A* co-dependency score of all

Fig. 1 | Mitotic checkpoint-dependency screen identifies the SKA complex. **A** Mean percentage ± standard deviation (SD) of pH3-positive mitotic cells measured by flow cytometry in RPE1-*hTERT*-iCas9 Δ*TP53* (WT), RPE1-*hTERT*-iCas9 Δ*TRIP13*Δ*TP53* (Δ*TRIP13*), and RPE1-*hTERT*-iCas9 Δ*TRIP13*Δ*TP53* + *pCMV-TRIP13* (Δ*TRIP13* + p*CMV-TRIP13*) cells after 18-hour nocodazole (Noco) treatment. $n = 3$ biologically independent experiments, each with technical duplicates. **B** Genome-wide single-cell copy-number profiles of WT ($n = 36$) and Δ*TRIP13* ($n = 42$) cells. Rows, cells; columns, chromosomes. Copy-number states are color-coded as indicated. Aneuploidy/karyotype heterogeneity scores were 0.079/0.043 for WT and 0.096/0.055 for Δ*TRIP13* cells. **C** Volcano plot of genes whose loss causes synthetic lethality (SL) or synthetic viability (SV) in Δ*TRIP13* relative to WT cells in the CRISPR screen. Significant hits (FDR < 0.1) are dark gray. **D** Relative viability after CRISPR knockout. $n = 3$ biologically independent experiments, each with technical triplicates. Bars show mean ± SD. $^{*}P = 0.012$ for cr*SKA1*, $^{*}P = 0.0155$ for cr*SKA2*. **E** Relative viability after CRISPR knockout and 25 nM Reversine. $n = 3$ biologically independent experiments, each with technical triplicates. Bars show mean ± SD. $^{***}P = 0.0001$. **F** Representative live-cell images after siMock or siSKA2, stained with a live-cell DNA probe. Across $n = 3$ biologically independent experiments, 169, 178, 221, and 195 cells were analyzed for WT siMock, WT siSKA2, Δ*TRIP13* siMock, and Δ*TRIP13* siSKA2, respectively. Cell fates: blue, completed mitosis; yellow, no mitotic exit; teal, aberrant anaphase; purple, mitotic death. Asterisks mark aberrancies. Time, hours:minutes. Scale bar, 10 µm. **G** Quantification of mitotic cell fates of the cells described in (**F**). **H** Mitotic exit timing after siMock or siSKA2. Cells were tracked > 20 h, no mitotic exits occurred after 6 h. Only cells observed entering mitosis were included. Curves show mean percentage across three biologically independent experiments, shading indicates standard error. $n = 165$, 130, 218, and 189 cells for WT siMock, WT siSKA2, Δ*TRIP13* siMock, and Δ*TRIP13* siSKA2, respectively. Statistics: one-way ANOVA (**A**), two-way ANOVA (**D**, **E**), two-sided Fisher's exact test (**G**), and log-rank test (**H**), each with correction for multiple comparisons. $^{****}P < 0.0001$; ns, not significant. Source data are provided as a Source Data file.

genes (~18,000) investigated in the DepMap initiative. Reciprocal co-dependency analyses using *SKA1-3* and *HAUS1-8* as query genes revealed similar relationships (Supplementary Fig. S7A–C and Supplementary Data 2B–L). These results recapitulate the differential viability effects observed in our SAC-deficiency screen. As mitotic checkpoint-dependent essentiality underlies the selective killing of chromosomally unstable cancer cells by KIF18A inhibition[7,8], this analysis implies that targeting such SV factors may expose comparable cancer-specific vulnerabilities.

KIF18A and the SKA complex are epistatic

To position the identified SAC-contingent SV factors in functional pathways relative to our top hits *SKA1-3*, we performed a second genetic screen in *ΔSKA1ΔTRIP13* cells (Supplementary Fig. S8A and Supplementary Data 1D). Comparing gene-loss effects in *ΔTRIP13* versus *ΔSKA1ΔTRIP13* cells allowed us to identify factors that genetically phenocopy or diverge from SKA complex loss alone (Fig. 2C). This can reveal genetic relationships with the SKAc, which may indicate shared phenotypic behavior. As expected from components of the same protein complex, loss of *SKA2* or *SKA3* had no differential effect in Δ*SKA1*Δ*TRIP13* cells (*i.e.*, their gene-loss effect became neutral, similar to the effect of targeting *SKA1*) (Fig. 2D). Most other SV factors behaved differently. Augmin complex components (*HAUS1, 3-5* and *8*), as well as *CSNK1A1, CUL3, MAGOH, PPP1R12A*, and *PPP1CB* shifted from synthetic viable in Δ*TRIP13* cells to synthetic lethal in Δ*SKA1*Δ*TRIP13* cells (Fig. 2D). These findings indicate that, contrary to *SKA1-3* loss, disruption of these factors causes additional – presumably mitotic – defects that negatively impact cellular viability in the absence of the SKAc. Unlike all other mitotic SV genes, *KIF18A* loss had no additional effect on viability once the SKAc was absent (i.e., *KIF18A* loss became neutral in Δ*SKA1*Δ*TRIP13* cells, mirroring the behavior of *SKA2* and *SKA3* (Fig. 2D)). In genetic terms, these data point to a unique epistatic relationship between *KIF18A* and *SKA1-3*.

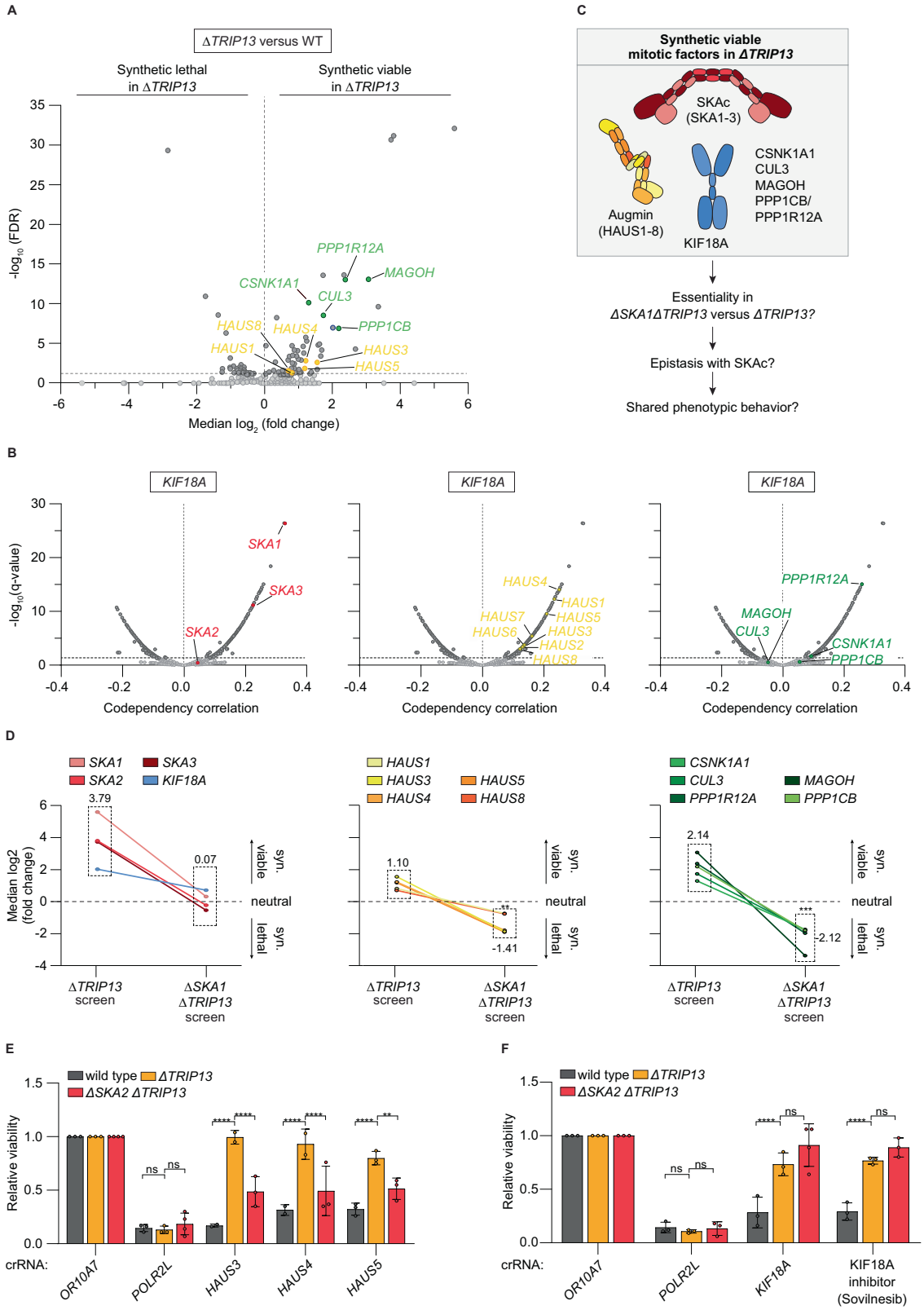
Confirming these analyses, viability of Δ*SKA2*Δ*TRIP13* or Δ*KIF18A*Δ*TRIP13* cells was decreased upon concurrent loss of Augmin subunits, *CSNK1A1, CUL3, MAGOH, PPP1R12A*, or *PPP1CB* (Fig. 2E and Supplementary Fig. S8B). In contrast, loss or chemical inhibition of *KIF18A* did not reduce cellular survival in Δ*SKA2*Δ*TRIP13* cells (Fig. 2F). Similarly, removal of *SKA2* in Δ*KIF18A*Δ*TRIP13* cells (Supplementary Fig. S8C) did not impact viability (Supplementary Fig. S8D). We conclude that, among the larger group of SAC-contingent SV factors, the SKA complex and KIF18A exhibit an epistatic relationship, indicating that the SKAc and KIF18A impact cellular survival in comparable ways.

The SKA complex is a vulnerability in chromosomally unstable cancer cells

Cancers that are aneuploid and/or exhibit CIN have a heightened dependence on KIF18A during mitosis, and the use of small-molecule inhibitors of KIF18A is currently being explored to combat cancers characterized by high levels of genome instability[8–15]. The identified genetic similarities between the SKA complex and KIF18A inspired us to focus on the SKA complex and investigate whether it represents a similar vulnerability in chromosomally unstable cancers. As large-scale dependency datasets do not typically capture ongoing chromosomal instability, we used aneuploidy status as a related feature to explore a possible association between SKAc dependence and chromosome instability. The association between cancer-associated aneuploidy and increased sensitivity to KIF18A loss has previously been established by dependency analysis in a large cohort of cancer cell lines[9–11]. We therefore analyzed genome-wide CRISPR dependency data from the CCLE[39]. Interestingly, stratification by aneuploidy status showed that the top 25% most aneuploid cancer cell lines were significantly more dependent on *SKA1* than the 25% most euploid cancer cell lines, mirroring their increased dependency on *KIF18A* (Fig. 3A and Supplementary Data 3A, B)[9]. Similar aneuploidy-associated dependence was observed for the complete SKAc (*SKA1-3*) (Fig. 3A and Supplementary Data 3M). Across the screened cancer cell lines, higher aneuploidy scores were modestly but significantly correlated with increased dependency on *SKA1* and *SKA3*, reflected by more negative dependency scores (Supplementary Fig. S9A and Supplementary Data 3B, 3D). Again, these effects were comparable to those seen for *KIF18A* (Supplementary Fig. S9B and Supplementary Data 3A). Most other SV hits showed no association with aneuploidy scores (Supplementary Fig. S9C, S9D and Supplementary Data 3C, 3E–R). These data show that, indeed, loss of the SKAc exposes a KIF18A-like cancer cell vulnerability, which is associated with aneuploidy levels across a large cohort of cancer cell lines.

We next experimentally tested whether SKAc loss mimics KIF18A inhibition in cancer cell lines[8,74]. To do so, we used a panel of colon (HCT-116, DLD-1), breast (HCC-1806), ovarian (OVCAR-3), and cervical (HeLa) cancer cell lines, previously shown to span a range of KIF18A inhibitor sensitivities and aneuploidy levels[8,74] (Fig. 3B and Supplementary Fig. S10A). Based on drug response curves to the KIF18A inhibitor Sovilnesib[58] (Fig. 3C, Supplementary Fig. S10B) that aligned with published data[8,74], we categorized HCT-116 and DLD-1 as insensitive cell lines, and HCC-1806, HeLa, and OVCAR-3 as sensitive. Consistent with the roles of the SKAc in mitosis[40–44,56,57], siRNA-mediated depletion of *SKA2* (Supplementary Fig. S10C) increased the mitotic fraction in all cell lines tested (Fig. 3D), although these effects were not consistently significant. Strikingly, viability of the KIF18Ai-insensitive cell lines remained at an average of 92% upon *SKA2* depletion, while it dropped to 27% in sensitive cell lines (Fig. 3E), mirroring the response to KIF18A inhibition (Fig. 3C)[8]. This differential sensitivity could not be attributed to different general efficacies of siRNA-mediated protein depletion, as knockdown of the essential factor *POLR2L* resulted in

https://doi.org/10.1038/s41467-026-79311-0



viability loss across all cell lines (Fig. 3E). Further, the effects were not caused by differences in baseline proliferation rates (Supplementary Fig. S10D), or by different intrinsic vulnerabilities to broad mitotic disruption, as *PLK1* knockdown reduced viability to below 15% in all cell lines (Fig. 3E). The fact that we observed mitotic fractions upon *SKA2* depletion while viability effects differed starkly across the panel of cell lines could indicate that *i) SKA2*-sensitive cells are more prone to cell death when arrested in mitosis, and/or ii) these cells delay for a longer time in mitosis (Fig. 3D, E), and further experiments should distinguish between these two scenarios.

Notably, depletion of other SV hits (*CSNK1A1, CUL3, MAGOH, PPP1R12A*, and *PPP1CB*) did not reproduce the SKA-like differential effects on viability or mitotic arrest in this cancer cell panel

Fig. 2 | Co-dependency and genetic epistasis between the SKA complex and KIF18A. A Volcano plot of mitosis-linked genes whose loss causes synthetic viability (SV) in RPE1-*hTERT*-iCas9-Δ*TRIP13*Δ*TP53* (Δ*TRIP13*) relative to RPE1-*hTERT*-iCas9-Δ*TP53* (WT) cells in the CRISPR screen. Significant hits (FDR < 0.1) are dark gray. **B** Volcano plots of *KIF18A* gene co-dependency correlations across cancer cell lines. The x-axis shows the Pearson correlation coefficient (r), the y-axis shows significance. Significant co-dependencies ($q < 0.05$) are dark gray. **C** Schematic of SAC-contingent synthetic viable factors and the rationale for the Δ*SKA1*Δ*TRIP13* versus Δ*TRIP13* setup to derive epistatic relationships. **D** Gene effects in the Δ*TRIP13* and Δ*SKA1*Δ*TRIP13* CRISPR screens, based on the mean abundance scores of four sgRNAs per gene. Plotted genes were significant synthetic viable hits in the Δ*TRIP13* screen, with a positive fold change in guide abundance. $n = 3$ technical replicates per screen. One-way ANOVA with correction for multiple comparisons, comparing each group of genes to the mean *SKA1-3* and *KIF18A* guide abundance in the Δ*SKA1*Δ*TRIP13* screen. $^{**}P = 0.0088$, $^{***}P = 0.0005$. **E** Relative viability after CRISPR knockout. $n = 2$ biologically independent experiments for WT/Δ*TRIP13* + cr*HAUS3* and cr*HAUS4*, and $n = 3$ for all other conditions, all with technical triplicates. Bars show mean ± standard deviation (SD). Two-way ANOVA with correction for multiple comparisons; $^{**}P = 0.0024$. **F** Relative viability after CRISPR knockout or chemical inhibition. $n = 4$ biologically independent experiments for Δ*SKA2*Δ*TRIP13* + cr*KIF18A* and $n = 3$ for all other conditions, all with technical triplicates. Bars show mean ± SD. Two-way ANOVA with correction for multiple comparisons. $^{****}P < 0.0001$; ns, not significant. Source data are provided as a Source Data file.

(Supplementary Fig. S10E, F). This reinforces our prior epistasis analysis that isolated the SKAc as a unique KIF18A-like factor among a larger group of SAC-contingent mitotic genes.

We tested a direct connection between SKAc dependence and chromosome ploidy. For this, we transiently treated a population of near-diploid HCT-116 cells with the MPS1 inhibitor Reversine (Fig. 3F). Pulsed MPS1 inhibition causes reversible SAC deficiency and increases levels of chromosome missegregation[55], leading to the generation of cell populations with heterogeneous, complex karyotypes[75]. Interestingly, depletion of *SKA2* in these Reversine-treated cells caused a significant decrease in cell viability, as compared to 'isogenic' untreated HCT-116 cells (Fig. 3G). Taken together, these data indicate that the mitotic SKA complex is a cellular vulnerability in chromosomally unstable cancer cells.

The SKA complex and KIF18A differentially impact chromosome alignment in mitosis

Considering the similar impact of interference with the SKAc and KIF18A on cellular viability and mitotic defects, we investigated how these factors mechanistically relate to each other during mitosis. SKA proteins and KIF18A exhibit proximity at kinetochores during (pro) metaphase[76,77]. SKAc localization at kinetochores was maintained in *ΔKIF18AΔTRIP13* cells, and KIF18A remained robustly associated with kinetochore microtubules in *ΔSKA2ΔTRIP13* cells (Fig. 4A and Supplementary Fig. S11A). In each case, signal was absent in the corresponding knockout line, confirming specificity. These observations indicate that these proteins localize independently, supporting a model in which the SKAc and KIF18A interact functionally through kinetochore-microtubule mechanics rather than via direct, reciprocal recruitment.

To understand why the SKAc and KIF18A behave similarly genetically, we compared their mitotic phenotypes. Consistent with its established roles in suppressing chromosome oscillations, promoting chromosome alignment, and suppressing microtubule growth[7,77], loss of KIF18A significantly increased chromosome spread in metaphase (measured as metaphase plate width and full width at half maximum of the metaphase plate) in Δ*TRIP13* cells (Fig. 4B and Supplementary Fig. S11B, C). Prolonging mitosis by a 30-minute metaphase arrest with the proteasome inhibitor MG-132 did not rescue this chromosome alignment defect (Fig. 4B and Supplementary Fig. S11C). KIF18A loss also significantly increased spindle length (Fig. 4C and Supplementary Fig. S11C). In contrast, loss of SKA2 had only modest effects on chromosome alignment, which were largely normalized following mitotic prolongation with MG-132 (Fig. 4B and Supplementary Fig. S11C). Loss of SKA2 also reduced the average spindle length during unperturbed mitosis (Fig. 4C and Supplementary Fig. S11C). Together, these results show that SKAc loss does not completely phenocopy KIF18A loss. Notably, deletion of *SKA2* in the *ΔTRIP13* background markedly reduced the severe chromosome alignment defects caused by acute KIF18A inhibition (Fig. 4B and Supplementary Fig. S11C). This suppression occurred independently of mitotic prolongation. Thus, although SKAc and KIF18A loss have similar effects on cell viability, they do not disrupt mitosis in the same way. Rather, our data indicate that the SKA complex is required for the full manifestation of the chromosome alignment defects caused by KIF18A loss. These observations reinforce the current model that while the SKA complex is needed to stabilize end-on kinetochore-microtubule attachments and to promote persistent coupling to dynamic microtubule tips[40–44,56,57], KIF18A is essential for microtubule dynamics, suppression of chromosome oscillations, and coordinated kinetochore-microtubule interactions[7,77]. Taken together, our data indicate that the SKAc and KIF18A have opposing contributions to microtubule-kinetochore attachments and thus stable chromosome alignment. These observations may explain their epistatic genetic relationship.

Prolonged mitosis exposes the SKA complex as a cellular vulnerability

Our data indicate that the mitotic SKAc function is molecularly distinct from that of KIF18A and that SKAc loss may even suppress KIF18A loss-associated defects in chromosome alignment. However, the loss of these factors exposes highly similar cellular vulnerabilities. Based on our analyses and the known roles of the SKAc, we consider it likely that the effects of SKAc loss originate from mitotic defects that are specifically exposed in chromosomally unstable cancer cells. In such cancer cells, cellular sensitivity to KIF18A inhibition is linked to molecular rewiring of mitotic control[8]. This altered behavior manifests as prolonged metaphase duration, likely driven by the altered balance between SAC and APC/C activities. We therefore explored whether prolonging metaphase, via interference with APC/C activity using proTAME[78], impacted cellular viability and chromosome segregation in Δ*SKA2*Δ*TRIP13* cells. Indeed, Δ*SKA2*Δ*TRIP13* cells were significantly more sensitive to partial APC/C inhibition, with an IC_{50} shift from 5.2 μM in Δ*TRIP13* to 2.3 μM in Δ*SKA2*Δ*TRIP13* cells (Fig. 4D). Live-cell imaging following proTAME treatment (Supplementary Fig. S11D) revealed a three-fold increase in mitotic cell death and more than a doubling of aberrant anaphases in Δ*SKA2*Δ*TRIP13* cells compared to Δ*TRIP13* alone upon induction of a mitotic delay (Fig. 4E, F, Supplementary Fig. S11E and Supplementary Movie 17, 18). These findings indicate that while SAC deficiency permits mitotic progression despite SKA complex loss, SAC-deficient cells remain sensitive to elongated metaphases. This direct connection between SKA dependency and interference with APC/C activity mirrors behavior observed upon KIF18A inhibition[8]. Combined, these experiments identify the SKAc as a novel vulnerability of chromosomally unstable cancer cells that is exposed in cells experiencing prolonged mitosis.

The development of resistance to small molecule-based anticancer drugs, including KIF18A inhibitors[79], is common[80]. Because our findings position the SKAc as a KIF18A-like vulnerability with distinct mitotic roles, we asked whether cancer cells with acquired resistance to a KIF18A inhibitor (Sovilnesib) maintained a heightened dependence on the SKAc. Through serial passaging under increasing concentrations of Sovilnesib, we acquired HeLa cells that are resistant to 125 nM Sovilnesib (Fig. 4G and Supplementary Fig. S11F). These resistant HeLa cells remained highly dependent on SKAc function, as judged by the impact of *SKA2* depletion on cellular viability (Fig. 4H).

https://doi.org/10.1038/s41467-026-79311-0

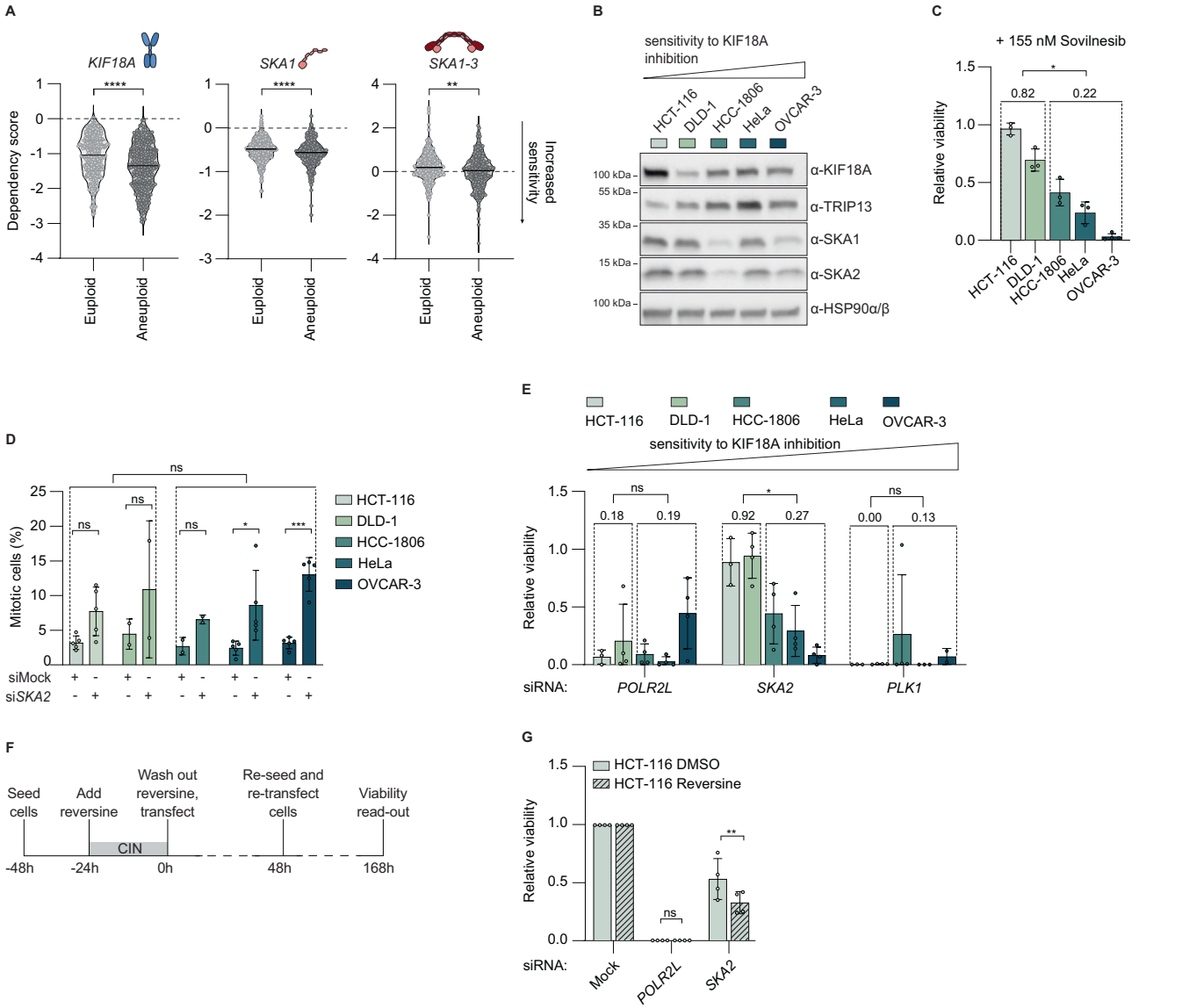


Fig. 3 | The SKA complex is a cellular vulnerability in chromosomally unstable cancer cells. A Sensitivity of near-euploid and highly aneuploid cancer cell lines to loss of *KIF18A* (left), *SKA1* (middle), or *SKA1-3* (right) in the Chronos CRISPR-Cas9 dataset. More negative dependency scores indicate greater gene essentiality. Medians are indicated. $^{**}P = 0.0011$. **B** Western blot of KIF18A, TRIP13, SKA1, and SKA2 in cancer cell lines with differing sensitivity to KIF18A inhibition. Representative of $n = 3$ biologically independent experiments. **C** Relative viability of cancer cell lines with differing sensitivity to KIF18A inhibition after 155 nM Sovilnesib treatment. $n = 3$ biologically independent experiments for HCT-116, DLD-1, HCC-1806, and HeLa, and $n = 4$ for OVCAR-3, all with technical triplicates. Bars show mean ± standard deviation (SD). $^{*}P = 0.041$. **D** Percentage of pH3-positive mitotic cells measured by flow cytometry after siMock or siSKA2 for 60 h, grouped as KIF18A-inhibition-insensitive (HCT-116, DLD-1) or -sensitive (HCC-1806, HeLa, OVCAR-3). $n = 2$ biologically independent experiments for DLD-1 and HCC-1806, and $n = 5$ for HCT-116, HeLa, and OVCAR-3, all with technical duplicates. Bars show mean ± SD. Group comparison is based on the mitotic fraction after siSKA2 treatment. $^{*}P = 0.0247$, $^{***}P = 0.0002$. **E** Relative viability after POLR2L, SKA2, or PLK1 depletion, grouped as KIF18A-inhibition-insensitive (HCT-116, DLD-1) or -sensitive (HCC-1806, HeLa, OVCAR-3). $n = 3$ biologically independent experiments for HCT-116 and $n = 4$ for all other cell lines, all with technical triplicates. Bars show mean ± SD. $^{*}P = 0.0195$. **F** Schematic of the workflow to assess viability after induction of chromosomal instability by pulsed MPS1 inhibition with Reversine. **G** Relative viability of HCT-116 cells after pulsed DMSO or 125 nM Reversine treatment. $n = 4$ biologically independent experiments, each with technical triplicates. Bars show mean ± SD. $^{**}P = 0.007$. Statistical significance was assessed by two-sided unpaired *t* test (**A**), nested two-sided *t* test (**C**, **E**), two-way ANOVA with correction for multiple comparisons (**D**, **G**), and nested *t* test (**D**). $^{****}P < 0.0001$; ns, not significant. Source data are provided as a Source Data file.

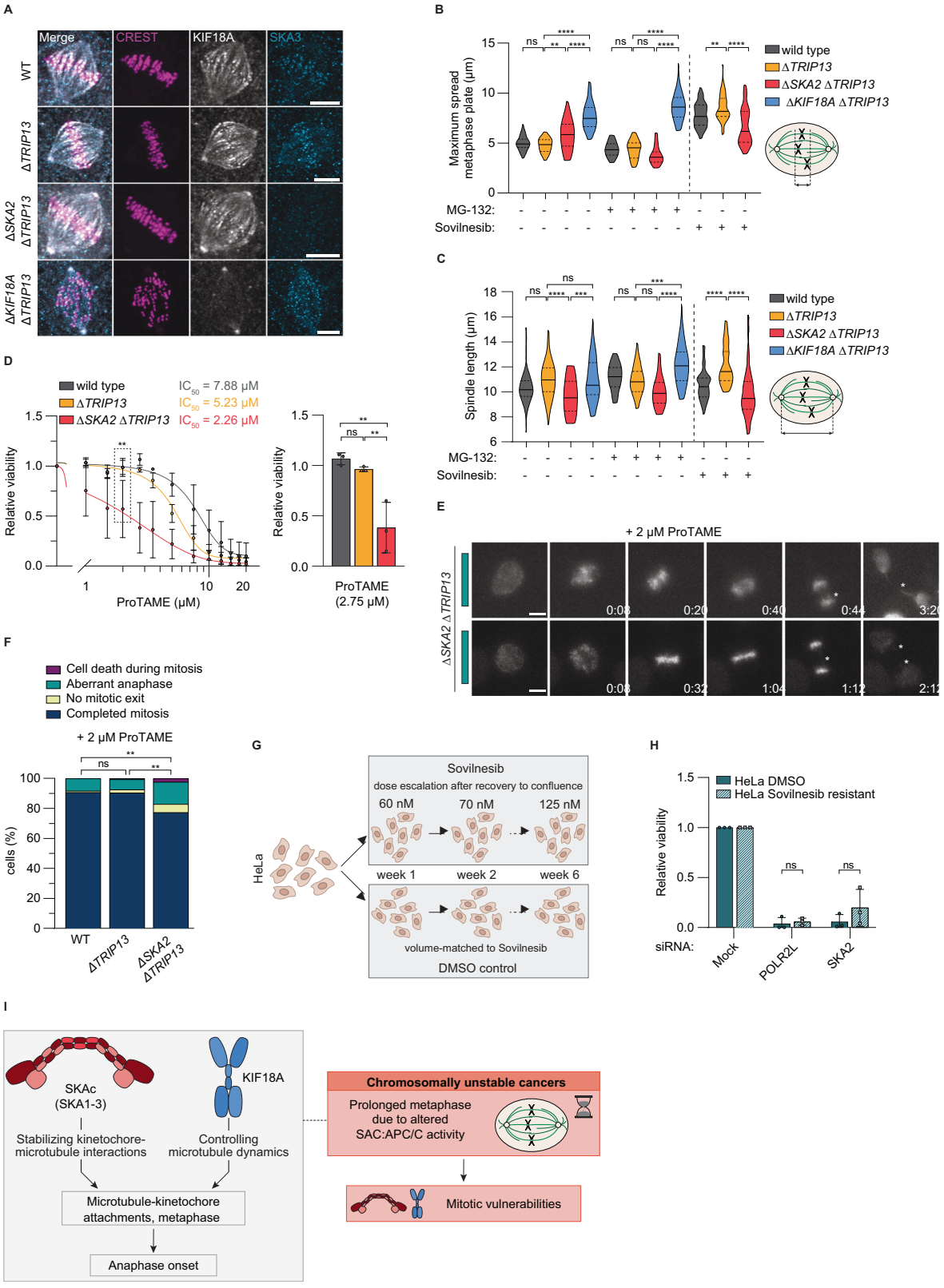
Thus, even in cells that do not respond to KIF18A inhibitors, the SKAc remains a mitotic vulnerability.

Discussion

Using genetic perturbations, we identify a class of mitotic regulators that becomes essential only when the spindle assembly checkpoint (SAC) is intact. This finding suggests that the mitotic defects caused by loss of such factors are not intrinsically lethal but only become detrimental when checkpoint engagement prolongs mitosis. Among these factors is the kinesin KIF18A, which has recently emerged as a selective mitotic vulnerability in chromosomally unstable cancers[8–11].

Our analyses in both non-transformed and cancer cell models identify the SKA complex as a KIF18A-like dependency (Fig. 4I). Like KIF18A, the SKAc is dispensable when the mitotic checkpoint is disabled but required when SAC signaling is intact. In addition, we found that time spent in mitosis (and specifically metaphase duration) impacts SKAc dependence. Genetically, the SKAc and KIF18A behave epistatically. Consistent with this connection, analysis of CRISPR

https://doi.org/10.1038/s41467-026-79311-0



dependency data from a large cohort of cancer cell lines reveals that SKAc dependency is associated with elevated aneuploidy levels, paralleling previous observations for KIF18A[8]. We corroborate this association experimentally. In total, we demonstrate that heightened dependency on the SKAc is set by a combination of imbalanced chromosome numbers, altered SAC function and increased mitotic duration, all characteristics of chromosomally unstable cancers[5–8]. As such, determinants of SKAc dependence parallel those that establish reliance on KIF18A[8]. Other genetic conditions, such as Rb pathway inactivation, contribute to KIF18A dependence[81], and it will be important to explore whether similar connections exist with SKAc dependence.

Although the SKAc and KIF18A impact kinetochore-microtubule interactions through molecularly distinct mechanisms, we find that

Fig. 4 | Differential impact of the SKA complex and KIF18A on cell division, with SKA complex-deficient defects exacerbated by prolonged mitosis. A Images of RPE1-*hTERT*-iCas9-Δ*TP53* (WT), RPE1-*hTERT*-iCas9-Δ*TRIP13*Δ*TP53* (Δ*TRIP13*), RPE1-*hTERT*-iCas9-Δ*SKA2*Δ*TRIP13*Δ*TP53* (Δ*SKA2*Δ*TRIP13*), and RPE1-*hTERT*-iCas9-Δ*KIF18A*Δ*TRIP13*Δ*TP53* (Δ*KIF18A*Δ*TRIP13*) cells stained for CREST (magenta), KIF18A (white), and SKA3 (cyan). Representative of $n = 3$ biologically independent experiments. Scale bar, 5 µm. **B** Maximum metaphase plate spread after DMSO, MG-132, or Sovilnesib. $n = 49/53/40/48$, 45/30/38/46, and 52/49/36 cells, respectively (order as in (**A**); Sovilnesib excludes Δ*KIF18A*Δ*TRIP13*). $^{**}P = 0.0013$ for Δ*TRIP13* vs Δ*SKA2*Δ*TRIP13*; $^{**}P = 0.0098$ for Sovilnesib-treated Δ*TRIP13* vs Δ*SKA2*Δ*TRIP13*. **C** Spindle length under (**B**) conditions. $n = 49/54/40/47$, 45/30/38/46, and 49/47/36 cells, respectively. $^{***}P = 0.0005$ for Δ*SKA2*Δ*TRIP13* vs Δ*KIF18A*Δ*TRIP13*, $^{***}P = 0.0006$ for MG-132-treated Δ*TRIP13* vs Δ*KIF18A*Δ*TRIP13*. **B**, **C** Medians/quartiles indicated, $n = 4$ biologically independent experiments for DMSO-treated WT, Δ*TRIP13*, Δ*KIF18A*Δ*TRIP13*; MG-132-treated WT; Sovilnesib-treated WT; $n = 3$ otherwise. (**D**) ProTAME dose-response and relative viability at 2.75 µM. Dashed lines: 2 µM, used subsequently. $n = 3$ biologically independent experiments with technical triplicates; mean ± standard deviation (SD). $^{**}P = 0.001$ (left), $^{**}P = 0.0034$ for WT vs Δ*SKA2*Δ*TRIP13* and $^{**}P = 0.0076$ for Δ*TRIP13* vs Δ*SKA2*Δ*TRIP13* (right). **E** Live-cell images of aberrant anaphases of Δ*SKA2*Δ*TRIP13* cells after 2 µM ProTAME. Representative of $n = 3$ biologically independent experiments. Asterisks mark aberrancies. Time, hours:minutes. Scale bar, 10 µm. **F** Mitotic fates after 2 µM ProTAME. $n = 194/281/186$ cells for WT, Δ*TRIP13*, and Δ*SKA2*Δ*TRIP13*, respectively, across three biologically independent experiments. $^{**}P = 0.0007$ for WT vs Δ*SKA2*Δ*TRIP13*; $^{**}P = 0.0014$ for Δ*TRIP13* vs Δ*SKA2*Δ*TRIP13*. **G** Generation of 125 nM Sovilnesib-resistant HeLa cells and DMSO-treated controls. **H** Relative viability after siMock, siSKA2, or siPOLR2L. $n = 3$ biologically independent experiments with technical triplicates; mean ± SD. **I** Model of the SKA complex (SKAc) as a KIF18A-like mitotic vulnerability of chromosomally unstable cancer cells, influenced by mitotic duration. The SKAc and KIF18A impact chromosome alignment through distinct mechanisms. Statistics: two-way ANOVA (**B**–**D**, **H**), pairwise two-sided Fisher's exact test (**F**), all with multiple-comparison correction. $^{****}P < 0.0001$; ns, not significant. Source data are provided as a Source Data file.

SKAc loss, like KIF18A inhibition/loss, triggers mitotic checkpoint activation, which is specifically deleterious in cells with prolonged metaphase[8]. Indeed, defects in chromosome segregation caused by SKAc loss are tolerated when the SAC is disrupted but become more severe as mitotic duration increases. Together, these findings suggest that the selective importance of the SKAc in chromosomally unstable cancer cells arises from chromosome segregation defects that coincide with prolonged checkpoint-dependent mitosis.

The success of PARP inhibitors in the treatment of homologous recombination–deficient tumors demonstrates the value of targeting cancer-specific liabilities[82]. Given the widespread prevalence of chromosome imbalance in human cancers[83], mitotic vulnerabilities that arise selectively in chromosomally unstable cells may offer a similarly promising route for precision therapy. These cancers are characterized not only by altered chromosome number, but also by rewired mitotic control, including changes in SAC and APC/C activity. Our data suggest that loss of the SKA complex exposes this altered control as a cancer-specific vulnerability. Thus, we identify the SKA complex as a candidate therapeutic target in chromosomally unstable cancers. We note that our analyses position the SKAc in a mitotic pathway distinct from KIF18A and suggest that SKAc inhibition may prove to be effective as a therapeutic option even in circumstances of resistance to KIF18A inhibition.

Disrupting this structural complex will likely rely on partial or intermittent targeting, which may be enabled through the development of chemical tools such as PROTACs or molecular glues[84]. In vivo studies should establish whether particular tumor genotypes or levels of chromosomal instability confer enhanced sensitivity to (partial) SKAc inhibition, and whether such inhibition can be achieved while sparing normal proliferative tissues.

Methods

Cell culture

All RPE1 cells were grown in DMEM (Gibco) supplemented with 7.5% fetal bovine serum (FBS, Capricorn). HeLa cells were grown in Advanced DMEM/F-12 (Gibco) with 9% FBS and 1% GlutaMAX (Gibco). OVCAR-3 cells were grown in RPMI 1640 (Gibco) with 20% FBS and 10.6 µg/mL human insulin (Sigma-Aldrich). HCT-116 cells were grown in McCoy's 5 A (Modified) Medium (Gibco) with 9% FBS and 1% GlutaMAX (Gibco). DLD-1 and HCC-1806 cells were grown in RPMI 1640 (Gibco) with 9% FBS. All cell culture media were supplemented with 1% penicillin-streptomycin (Gibco). All cell lines were grown at 37 °C under 5% CO_2 and routinely tested negative for mycoplasma contamination. RPE1-*hTERT*-iCas9-Δ*TP53* cells were described previously[85]. CRISPR-Cas9 genome editing was used to generate RPE1-*hTERT*-iCas9-Δ*TRIP13*Δ*TP53*, RPE1-*hTERT*-iCas9-Δ*SKA1/2/3*Δ*TRIP13*Δ*TP53* and RPE1-*hTERT*-iCas9-Δ*TP53*-Δ*KIF18A*Δ*TRIP13* cell lines. Edited cell pools were seeded at low density, after which single-cell clones were isolated and validated by TIDE analysis[86] and western blotting. Primer sequences are listed in Supplementary Table 1. Sovilnesib-resistant HeLa cells were generated by continuous exposure of parental cells to gradually increasing concentrations of Sovilnesib over a period of six weeks. Cells were initially treated with 60 nM, and the concentration was increased to 75, 90, 100 and 125 nM once cells had recovered and reached confluence at each concentration. If cells did not reach confluence within three or four days, the culture medium with inhibitor was refreshed. Cells were continuously maintained in the presence of the drug throughout the selection period and once resistant to 125 nM Sovilnesib. In parallel, an isogenic control population was cultured under the same conditions using volume-matched DMSO. HCT-116 cells were kindly provided by Geert Kops (Hubrecht Institute), and OVCAR-3 cells by Marcel van Vugt (University Medical Center Groningen).

CRISPR-Cas9 genome editing

All genome editing was performed in cell lines containing an inducible Tet-On Cas9 expression system. One day before transfection, cells were seeded, and Cas9 expression was induced with 200 ng/mL doxycycline. Transfections were performed using Lipofectamine RNAiMAX (Invitrogen) at a 1:1000 dilution with equimolar concentrations of crRNA and tracrRNA (IDT) in OptiMEM (Gibco), to a final concentration of 50 nM crRNA:tracrRNA duplex per 40,000 cells. crRNA sequences are listed in Supplementary Table 2. Editing efficiencies were assessed through TIDE analysis after Sanger sequencing, primer sequences are listed in Supplementary Table 1.

Lentiviral transduction

To generate the RPE1-hTERT-iCas9-Δ*TRIP13*Δ*TP53* + pCMVie-TRIP13 cell line (referred to as Δ*TRIP13* + *pCMV-TRIP13*), TRIP13 was re-expressed via lentiviral transduction. TRIP13 cDNA was cloned into pLenti CMVie-IRES-BlastR, a gift from Ghassan Mouneimne (Addgene plasmid #119863). Lentiviral particles were produced in HEK293T cells and used to transduce the RPE1-hTERT-iCas9-Δ*TP53*Δ*TRIP13* cells. Transduced cells were selected with 10 µg/mL blasticidin, and TRIP13 expression was confirmed by western blotting.

RNA interference

siRNA-mediated knockdown of target genes was achieved by transfecting cells with a final concentration of 20 nM ON-TARGETplus siRNA SMARTPools (Dharmacon Reagents) using Lipofectamine RNAiMAX at a 1:1000 dilution. Analysis or re-seeding of cells was performed 48 h post-transfection unless stated otherwise. Gene knockdown was validated by western blotting. Target sequences included *ANAPC15* (L-020237-02-0005), *CSNK1A1* (L-003957-00-0005), *CUL3* (L-010224-00-

0005), *HAUS3* (L-018131-01-0005), *MAGOH* (L-011327-00-0005), *PLK1* (L-003290-00-0010), *POLR2L* (L-013133-01-0020), *PPP1CB* (L-008685-00-0005), *PPP1R12A* (L-011340-00), and *SKA2* (L-018781-01-0005). A non-targeting (NT) siRNA pool was used as a negative control (D-001810-01-20).

Genome-wide CRISPR-Cas9 screen

The Δ*TRIP13* genome-wide CRISPR-Cas9 screen was performed in RPE1-*hTERT*-iCas9-Δ*TRIP13*Δ*TP53* cells, which form an isogenic pair to the RPE1-*hTERT*-iCas9-Δ*TP53* cells previously screened, as described in ref. 85. The Δ*SKA1*Δ*TRIP13* screen was performed using RPE1-*hTERT*-iCas9-Δ*SKA1*Δ*TRIP13*Δ*TP53* and RPE1-*hTERT*-iCas9-Δ*TRIP13*Δ*TP53* cells. During the screens, all cells were grown in DMEM medium (Gibco) supplemented with 9% fetal bovine serum, 1% penicillin-streptomycin (Gibco), 1% sodium pyruvate (Gibco) and 0.5 µg/mL Amphotericin B (Gibco). The screens were performed using the TKOv3 library[87] at a 400-fold library representation, in triplicate. Cells were transduced with pLCKO-TKOv3 in medium containing 8 µg/mL polybrene at an MOI of approximately 0.2. Medium was refreshed after 24 h, and 5 µg/mL puromycin was added to select for transduced cells. After three days of selection, cells were divided into three independent populations, harvested for the $t = 0$ sample, and then reseeded in medium containing 200 ng/mL doxycycline to induce Cas9 expression. Cells were passaged every three population doublings, which corresponded to every three days, for a total of twelve population doublings. Doxycycline was maintained in the medium throughout culturing. Genomic DNA was isolated from cell pellets using the Blood and Cell Culture DNA Maxi Kit (Qiagen), and integrated sgRNA sequences were amplified by PCR using KAPA HiFi HotStart ReadyMix (Roche). Lentiviral inserts were amplified by PCR, and Illumina adapters and i5 and i7 index sequences were added in two PCR steps as described previously[85]. The triplicates from the different samples ($t = 0$ and $t = 4$) were pooled and sequenced on a NovaSeq6000 (Illumina). Sequences were mapped to the TKOv3 library (not allowing any mismatches), and the differential gRNA count data were analyzed and attributed to gene scores using IsogenicZ, an adapted version of DrugZ optimized for isogenic cell line screens, using a previous screen in the RPE1-Δ*TP53* parental cell line as a control[85,88,89].

GOterm analysis

The hits identified in the CRISPR-Cas9 screen were analyzed for gene ontology (GO) enrichment using the GO Ontology database (DOI: 10.5281/zenodo.15066566, released 2025-03-16)[90,91] and https://string-db.org/[92,93].

Chemical compounds

All chemical compounds were dissolved in DMSO and used at the indicated concentrations unless otherwise specified. Nocodazole (Sigma-Aldrich M1404) was used at a final concentration of 0.3 µM for 18 h to arrest cells in mitosis. Palbociclib (Selleck Chem S1116) was used at a final concentration of 200 nM for 24 h to synchronize cells in G1 phase. RO-3306 (Sigma-Aldrich #217699) was used at 9 µM for 18 h to synchronize cells at the G2/M transition. MG-132 (Sigma-Aldrich C2211) was used at a final concentration of 5 µM to arrest cells in metaphase. ProTAME (Sigma-Aldrich SML3977) was used in varying concentrations to inhibit the APC/C. Sovilnesib, a KIF18A inhibitor developed by Amgen and kindly provided to us by M. Luijsterburg (LUMC), was used at 125 nM to inhibit KIF18A activity unless stated otherwise. Reversine (Sigma-Aldrich R3904) was used in varying concentrations to inhibit MPS1 and thus the spindle assembly checkpoint.

Viability and clonogenic assays

Cells were seeded two days after transfection with crRNA:tracrRNA duplexes. For viability assays, cells were seeded in 96-well plates at a density of 500 cells per well, with an exception for OVCAR-3 cells, which were seeded at a density of 1500 cells per well. Seven days post-transfection, the culture medium was replaced with medium containing 40 µM Resazurin (Sigma-Aldrich). After a four-hour incubation at 37 °C, fluorescence was measured at 545 nm excitation/600 nm emission using a CLARIOstar Plus plate reader (BMG Labtech). Fluorescence measurements were corrected for background fluorescence from wells containing medium only. For clonogenic assays, cells were seeded two days post-transfection in 6-well plates at a density of 1000 cells per well. Twelve days after transfection, cells were stained using 0.5 mg/mL crystal violet solution (Merck) with 20% MeOH.

Drug response assays

Cells were seeded in 96-well plates at a density of 500 cells per well, with an exception for OVCAR-3 cells, which were seeded at a density of 1500 cells per well, one day prior to drug treatment. Three days post-treatment, the culture medium was refreshed, and fresh drug was added. Seven days after initial drug addition, the culture medium was replaced with medium containing 40 µM Resazurin (Sigma-Aldrich). After a four-hour incubation at 37 °C, fluorescence was measured at 545 nm excitation/600 nm emission using a CLARIOstar Plus plate reader (BMG Labtech). Fluorescence measurements were corrected for background fluorescence from wells containing medium only.

Western blotting

For western blotting, cells were lysed in lysis buffer (50 mM Tris-HCl pH 7.4, 150 mM NaCl, 1% Triton X-100 supplemented with fresh protease and phosphatase inhibitors) for ten minutes on ice and centrifuged at 4 °C and 18,400 x *g* for ten minutes. Proteins were separated on 4–15% Mini-PROTEAN TGX Precast Protein gels (Bio-Rad), followed by a semi-dry transfer to a nitrocellulose membrane (Bio-Rad). After blocking in 5% milk in TBS-T for 30 min, membranes were incubated at 4 °C overnight with the following primary antibodies at the indicated dilutions in 5% milk in TBS-T: mouse α-HSP90$_{\alpha/\beta}$ (Biolegend 675402, 1:9000), rabbit α-KIF18A (Bethyl A301-080A, 1:1000), mouse α-MAD2 (Sigma-Aldrich MABE866, 1:1000), mouse α-P31^{COMET} (Sigma-Aldrich MABE451, 1:2000), rabbit α-REV7 (Abcam Ab180579, 1:1000), rabbit α-TRIP13 (Bethyl A303-605A, 1:1000), mouse α-Vinculin (Santa Cruz sc-25336, 1:1000). Polyclonal rabbit α-SKA1, α-SKA2, and α-SKA3 antibodies (described in ref. 44, 1:2000) were kindly gifted by Iain Cheeseman (Whitehead Institute for Biomedical Research). Following primary antibody incubation, membranes were incubated with HRP-conjugated secondary antibodies for one hour at room temperature: goat α-mouse (Cell Signaling 7074, 1:5000) and goat α-rabbit (Cell Signaling 7076, 1:5000). Proteins were visualized using Clarity Western ECL Substrate (Bio-Rad). Quantification of intensity levels was performed using ImageJ, taking the mean gray intensity for the relevant bands and subtracting background intensity. Original, uncropped scans of all western blots are included in the Source Data file.

Immunofluorescence and image analysis

Cells were seeded on 35-mm glass-bottom dishes with #1.5 (0.17 mm) cover glass thickness (MatTek Corporation) in 1 mL DMEM supplemented as described above to reach 80% confluence the following day. Where noted, cells were treated for 1 h prior to fixation with either DMSO or 250 nM Sovilnesib (MedChemExpress, HY-132840). Where indicated, cells were additionally treated 30 min prior to fixation with 5 µM MG-132 (Merck, M7449).

Cells stained for α-tubulin, CREST, and CENP-E were fixed for 2 min in ice-cold methanol (−20 °C). For staining of CREST, KIF18A, and SKA3, cells were first rinsed for 10 seconds with pre-warmed (37 °C) cell extraction buffer (100 mM PIPES, 1 mM $MgCl_2$, 1 mM EGTA, 0.5% Triton X-100), followed by methanol fixation as described above. After fixation and three 5-minute PBS washes, cells were permeabilized with 0.5% Triton X-100 in water for 30 min at room temperature. To block nonspecific binding, cells were incubated in 1 mL blocking buffer

(2% normal goat serum, NGS; Thermo Fisher, 10000 C) for 2 h at room temperature. Cells were then washed three times for 5 min in PBS and incubated with 300 μL primary antibody solution overnight at 4 °C. Primary antibodies were diluted in PBS containing 0.1% Triton X-100 and 1% NGS. The following primary antibodies were used: rabbit anti-KIF18A (A301-080A, Bethyl Laboratories, 1:500), rabbit anti-CENP-E (C7488, Sigma, 1:500), mouse anti-SKA3 (sc-390326, Santa Cruz, 1:100), rat anti-α-tubulin YL1/2 (MA1-80017, Invitrogen, 1:500), and human anti-centromere (CREST) serum (15–234, Antibodies Incorporated, 1:500). After primary antibody incubation and a PBS wash, cells were incubated for 1 h at room temperature with 500 μL secondary antibody solution diluted in PBS containing 0.1% Triton X-100 and 1% NGS. Secondary antibodies were selected according to the species of the primary antibodies. For CENP-E, CREST, and α-tubulin staining, the following secondary antibodies were used: donkey anti-rat Alexa Fluor 647 (Abcam, ab150155, 1:500), goat anti-human DyLight 594 (Abcam, ab96909, 1:1000), and goat anti-rabbit Alexa Fluor 488 (Abcam, ab150073, 1:500), respectively. For KIF18A, SKA3, and CREST staining, the following secondary antibodies were used: donkey anti-rabbit Alexa Fluor 594 (Abcam, ab150064, 1:1000), donkey anti-mouse Alexa Fluor 488 (Abcam, ab150105, 1:500), and goat anti-human Alexa Fluor 647 (Jackson ImmunoResearch, 109-605-003, 1:1000), respectively. This was followed by washing three times 10 min in PBS. Cells were imaged immediately after staining or stored at 4 °C protected from light for up to one week prior to imaging.

Cells were imaged using a Zeiss LSM 800 laser scanning confocal microscope equipped with a Plan-Apochromat 63 ×/1.40 NA oil immersion objective (DIC M27). Images were acquired using ZEN Blue software (Zeiss). For tubulin–CENP-E staining experiments, images were acquired at 512 × 512 pixel resolution with a lateral sampling of 0.0495 μm per pixel and a z-step size of 0.5 μm, generating 31 optical sections per stack. Fluorescence signals were recorded sequentially using Alexa Fluor 488 (tubulin), Alexa Fluor 594 (CENP-E), and Alexa Fluor 647 (CREST) channels. Imaging was performed using unidirectional scanning (scan speed 14) with line averaging set to 1, and images were acquired as 8-bit datasets. For KIF18A–SKA3 staining experiments, images were acquired at 488 × 488 pixel resolution with a lateral sampling of 0.041 μm per pixel and a z-step size of 0.5 μm, generating 31 optical sections per stack. Fluorescence signals were recorded sequentially using Alexa Fluor 488 (SKA3), Alexa Fluor 594 (KIF18A), and Alexa Fluor 647 (CREST) channels. Imaging parameters were otherwise identical to those described above, and images were acquired as 16-bit datasets. Image stacks from these experiments were subsequently processed using the ZEN LSM Plus deconvolution algorithm (AutoWiener filter) prior to analysis. Z-stacks spanning approximately 15 μm were collected sequentially at multiple stage positions.

Image analysis was performed in Fiji. To quantify immunofluorescence intensities for KIF18A and SKA3, sum intensity projections encompassing the entire spindle volume were generated. Regions of interest (ROIs) were manually defined by encompassing CREST-labeled kinetochores, and the mean signal intensity was measured within these ROIs for the KIF18A and SKA3 channels. Background signal for each channel was determined by averaging intensity measurements from two independent cytoplasmic locations per cell and was subsequently subtracted from the signal measured at the CREST-labeled region. To minimize technical variation, all replicates were processed in parallel, fixed, immunostained, and imaged on the same day using identical imaging parameters. Finally, intensity values were normalized to the mean value of RPE1-*hTERT*-iCas9 *ΔTP53* cells within each respective replicate. Spindle length was measured in maximum-intensity projection images as the distance between the tubulin foci corresponding to the two spindle poles. Multipolar and highly tilted spindles were not imaged. In the analyzed dataset, spindle poles were separated by no more than eight z-planes. Maximum metaphase plate spread was quantified as the distance between the outermost CREST signals along the main spindle axis. A fixed-size oval region of interest (ROI) was used for all measurements, with the ROI size corresponding to the CREST kinetochore signal. Background intensity was measured in the cytoplasm at three independent locations, averaged, and subtracted from the kinetochore signal. For full width at half maximum (FWHM) measurements, a Gaussian blur ($\sigma = 1$) was applied before analysis. To quantify kinetochore alignment along the spindle axis using an independent metric, intensity profiles of CREST signals were analyzed in Fiji, as described before[94]. Briefly, a 200-pixel linear ROI was drawn along the main spindle axis, and gray-value intensities were extracted. Intensity profiles were centered on the metaphase plate. Spatial coordinates were converted from pixels to micrometers (μm) prior to analysis. The FWHM of the CREST signal was used as a quantitative measure of kinetochore alignment. For each profile, the half-maximum threshold was defined as $y_{hm} = (y_{max} + y_{min})/2$, where y_{max} represents the global maximum intensity and y_{min} the local background baseline. The positions at which the signal crossed this threshold (x_{left} and x_{right}) were determined by linear interpolation between adjacent data points to obtain sub-pixel accuracy. The FWHM was then calculated as $FWHM = x_{right} - x_{left}$. Smaller FWHM values indicate tighter kinetochore clustering at the metaphase plate, whereas larger FWHM values or multimodal profiles indicate chromosome misalignment or spindle disorganization.

Flow cytometry

Upon harvesting the cells and culture supernatant, cells were rinsed in cold PBS with 0.05% EDTA, trypsinized, and washed with PBS before fixation in cold 70% ethanol. After incubation at − 20 °C for at least an hour, cells were permeabilized with 0.05% Tween-20 in PBS. Following a wash with 0.05% Tween-20 in PBS, cells were blocked and stained overnight at 4 °C using α-Histone H3 phospho-Serine 10-Alexa Fluor 647 (Biolegend 650806) diluted 1:100 in 0.05% Tween-20/2% BSA in PBS. After three washes with 0.05% Tween-20 in PBS, the cells were stained with 0.5 μg/mL DAPI in 0.05% Tween-20/2% BSA in PBS. Cells were analyzed using an LSRFortessa X-20 (BD Biosciences) or CytoFLEX LX Flow Cytometer (Beckman Colter). FlowJo software was used for data processing. To assess the fraction of mitotic cells, live-cells were first gated, followed by single cells gating. These were then gated for the pH3-positive, 4 N population.

Live-cell imaging

Cells were grown in 8-well Nunc Lab-Tek II Chambered Coverglasses (Thermo Scientific), with the addition of the appropriate chemical compounds needed for the experiment. Four hours prior to the start of imaging, SPY650-DNA (Spirochrome, 1:2000) and verapamil (Spirochrome, 1:10,000) were added to the cells. Imaging was performed every four minutes using a THUNDER Imager Live-cell (Leica Microsystems) equipped with an HC PL APO 20x/0.80 objective (dry) and a deep-cooled 4.2 MP sCMOS camera, with cells maintained at 37 °C under 5% CO_2. Image analysis was performed in Fiji based on maximum-intensity projection images. All scoring was performed blinded.

Chromosome spreads

Cells were treated with 200 ng/mL demecolcin for 20 minutes, harvested, and resuspended in 0.075 M KCl for 20 minutes. Subsequently, cells were fixed in methanol:acetic acid (3:1) and dropped onto glass slides. Following staining with 5% Giemsa solution, metaphases were assessed for chromosome numbers per cell.

Single cell karyotyping

Sequencing was performed using a NextSeq 2000 (Illumina; up to 74 cycles), after which the generated data were demultiplexed using sample-specific barcodes and changed into fastq files using bcl2fastq

(Illumina; version 1.8.4). Reads were aligned to the human reference genome (GRCh38/hg38) using Bowtie2 (version 2.2.4[95];) and duplicate reads were marked with BamUtil (version 1.0.3[96];). Copy number variation analysis was performed with AneuFinder (version 1.30.0; https://github.com/ataudt/aneufinder[97]). After GC correction and blacklisting of artifact-prone regions (extreme low or high coverage in control samples), libraries were analyzed using the dnacopy and edivisive copy number calling algorithms with variable width bins (average bin size = 1 Mb; step size = 500 kb) and breakpoint refinement (confint = 0.95). Blacklists and variable width bins were constructed using an euploid reference[98]. Results were curated by requiring a minimum concordance of 90% between the results of the two algorithms. Libraries with on average less than 10 reads per chromosome copy of each bin (2-somy: 20 reads, 3-somy: 30 reads, etc.) were discarded. This minimum number of reads is approximately 55,000 for a diploid genome. The aneuploidy score of each bin was calculated as the absolute difference between the observed copy number and the euploid copy number. The weighted average of the bins is the score per library, which was averaged to the score per sample. The heterogeneity score of each bin was calculated as the proportion of pairwise comparisons (cell 1 versus cell 2, cell 1 versus cell 3, etc.) that showed a difference in copy number (*e.g.*, cell 1: 2-somy and cell 2: 3-somy). The score of each sample is the weighted average of all bin scores.

DepMap analyses

For gene essentiality assessment, gene effect scores from the DepMap project were downloaded and analyzed ([99] and (https://depmap.org/portal/). Gene effect scores quantify how essential a gene is for a cancer cell line. A score close to −1 indicates a gene is likely essential, which means knocking it out significantly reduces cell viability. A score near 0 or above indicates that the gene is likely non-essential. Gene effect scores for Δ*TRIP13* SV genes were compared with the gene effect scores of all screened genes and with those that are classified as 'common essential' in DepMap.

Aneuploidy scores (AS) for human cancer cell lines were obtained from ref. 100. mRNA gene expression values and CRISPR dependency scores (DS; Chronos) were obtained from the DepMap25Q2release[39] (OmicsExpressionExpectedCountHumanAllGenes.csv, and CRISPRGeneEffect.csv, respectively). FPKM values were calculated by normalizing the read counts for each gene to both the total library size (in millions of mapped reads) and the gene length (in kilobases), as defined in the Ensembl Homo Sapiens reference annotation (GRCh38, release 112), following standard protocols. In analyses where cells were divided into aneuploid and near-euploid groups, the division was performed using the top and bottom quartiles of AS (Top: AS ≥ 21; Bottom: AS ≤ 8). Gene preferential essentiality in aneuploid versus near-euploid cells was calculated as the mean DS difference between groups, and associated *P*-values were derived from unpaired, two-tailed t-tests. Correlations between gene dependency and aneuploidy were assessed using Spearman's rank correlation coefficient (ρ), with *P*-values derived from two-tailed tests. Co-dependency analysis was performed using pairwise Spearman's correlation coefficients (ρ); corresponding *P*-values were computed using two-tailed tests and adjusted for multiple testing using the Benjamini–Hochberg false discovery rate (FDR) procedure to obtain Q-values. Results are displayed as $-\log_{10}$(Q-value) versus the correlation coefficient itself. Effect sizes were quantified using Cohen's d, calculated as the difference in means divided by the pooled standard deviation. In analyses assessing the *SKA1*, *SKA2*, and *SKA3* genes as a complex, SKA-complex expression was calculated as the average FPKM mRNA expression of the three genes in each cell line.

Reporting summary

Further information on research design is available in the Nature Portfolio Reporting Summary linked to this article.

Data availability

The raw single cell whole genome sequencing data generated in this study have been deposited at the European Nucleotide Archive (ENA) under accession number PRJEB127279. The CRISPR screen data generated in this study are provided in the Supplementary Data. The publicly available mRNA gene expression values and CRISPR dependency scores were obtained from the DepMap25Q2 release. All other data are provided in the manuscript, Supplementary Information, or Supplementary Data. Materials are available from the corresponding author as applicable. Source data are provided in this paper.

References

1. Kittler, R. et al. Genome-scale RNAi profiling of cell division in human tissue culture cells. *Nat. Cell Biol.* **9**, 1401–1412 (2007).
2. Kittler, R. et al. An endoribonuclease-prepared siRNA screen in human cells identifies genes essential for cell division. *Nature* **432**, 1036–1040 (2004).
3. Neumann, B. et al. Phenotypic profiling of the human genome by time-lapse microscopy reveals cell division genes. *Nature* **464**, 721–727 (2010).
4. Funk, L. et al. The phenotypic landscape of essential human genes. *Cell* **185**, 1–20 (2022).
5. Sacristan, C. & Kops, G. J. P. L. Joined at the hip: Kinetochores, microtubules, and spindle assembly checkpoint signaling. *Trends Cell Biol.* **25**, 21–28 (2015).
6. Musacchio, A. The molecular biology of spindle assembly checkpoint signaling dynamics. *Curr. Biol.* **25**, R1002–R1018 (2015).
7. Janssen, L. M. E. et al. Loss of Kif18A results in spindle assembly checkpoint activation at microtubule-attached kinetochores. *Curr. Biol.* **28**, 2685–2696 (2018).
8. Gliech, C. R. et al. Weakened APC/C activity at mitotic exit drives cancer vulnerability to KIF18A inhibition. *EMBO J.* https://doi.org/10.1038/s44318-024-00031-6 (2024).
9. Cohen-Sharir, Y. et al. Aneuploidy renders cancer cells vulnerable to mitotic checkpoint inhibition. *Nature* **590**, 486–491 (2021).
10. Marquis, C. et al. Chromosomally unstable tumor cells specifically require KIF18A for proliferation. *Nat. Commun.* **12**, 1213 (2021).
11. Quinton, R. J. et al. Whole-genome doubling confers unique genetic vulnerabilities on tumour cells. *Nature* **590**, 492–497 (2021).
12. National Library of Medicine (US). A study to investigate safety, tolerability, pharmacokinetics and preliminary efficacy with GenSci122 in participants with advanced solid tumors.https://clinicaltrials.gov/study/NCT06772415 (2025).
13. National Library of Medicine (US). A study of sovilnesib in subjects with ovarian cancer.https://www.clinicaltrials.gov/study/NCT06084416?term=kif18a&rank=3 (2025).
14. National Library of Medicine (US). A phase I/II study of VLS-1488 in subjects with advanced cancer.https://www.clinicaltrials.gov/study/NCT05902988 (2025).
15. National Library of Medicine (US). First-in-human study of ATX-295, an oral inhibitor of KIF18A, in patients with advanced or metastatic solid tumors, including ovarian cancer.https://clinicaltrials.gov/study/NCT06799065 (2025).
16. National Library of Medicine (US). A first-in-human study of MEN2501 in participants with platinum-resistant ovarian cancer.https://clinicaltrials.gov/study/NCT07226427 (2026).
17. Eytan, E. et al. Disassembly of mitotic checkpoint complexes by the joint action of the AAA-ATPase TRIP13 and p31comet. *Proc. Natl. Acad. Sci. USA* **111**, 12019–12024 (2014).
18. Kim, D. H. et al. TRIP13 and APC15 drive mitotic exit by turnover of interphase- and unattached kinetochore-produced MCC. *Nat. Commun.* **9**, 4354 (2018).

19. Wang, K. et al. Thyroid hormone receptor interacting protein 13 (TRIP13) AAA-ATPase is a novel mitotic checkpoint-silencing protein. *J. Biol. Chem.* **289**, 23928–23937 (2014).
20. Alfieri, C., Chang, L. & Barford, D. Mechanism for remodelling of the cell cycle checkpoint protein MAD2 by the ATPase TRIP13. *Nature* **559**, 274–278 (2018).
21. Mapelli, M., Massimiliano, L., Santaguida, S. & Musacchio, A. The Mad2 conformational dimer: structure and implications for the spindle assembly checkpoint. *Cell* **131**, 730–743 (2007).
22. Mapelli, M. et al. Determinants of conformational dimerization of Mad2 and its inhibition by p31comet. *EMBO J.* **25**, 1273–1284 (2006).
23. Ye, Q. et al. TRIP13 is a protein-remodeling AAA+ ATPase that catalyzes MAD2 conformation switching. *Elife* https://doi.org/10.7554/eLife.07367.001 (2015).
24. Ye, Q. et al. The AAA+ ATPase TRIP13 remodels HORMA domains through N-terminal engagement and unfolding. *EMBO J.* **36**, 2419–2434 (2017).
25. Yang, M. et al. p31comet Blocks Mad2 activation through structural mimicry. *Cell* **131**, 744–755 (2007).
26. Sudakin, V., Chan, G. K. T. & Yen, T. J. Checkpoint inhibition of the APC/C in HeLa cells is mediated by a complex of BUBR1, BUB3, CDC20, and MAD2. *J. Cell Biol.* **154**, 925–936 (2001).
27. Hardwick, K. G., Johnston, R. C., Smith, D. L. & Murray, A. W. MAD3 Encodes a novel component of the spindle checkpoint which interacts with Bub3p, Cdc20p, and Mad2p. *J. Cell Biol.* **148**,http://www.jcb.org (2000).
28. Izawa, D. & Pines, J. The mitotic checkpoint complex binds a second CDC20 to inhibit active APC/C. *Nature* **517**, 631–634 (2015).
29. Luo, X. et al. The Mad2 spindle checkpoint protein has two distinct natively folded states. *Nat. Struct. Mol. Biol.* **11**, 338–345 (2004).
30. Habu, T., Kim, S. H., Weinstein, J. & Matsumoto, T. Identification of a MAD2-binding protein CMT2 and its role in mitosis. *EMBO J.* **21**, 6419–6428 (2002).
31. Xia, G. et al. Conformation-specific binding of p31comet antagonizes the function of Mad2 in the spindle checkpoint. *EMBO J.* **23**, 3133–3143 (2004).
32. Tipton, A. R. et al. Identification of novel mitosis regulators through data mining with human centromere/kinetochore proteins as group queries. *BMC Cell Biol.* **13**, https://doi.org/10.1186/1471-2121-13-15 (2012).
33. Ma, H. T. & Poon, R. Y. C. TRIP13 Regulates Both the Activation and Inactivation of the Spindle-Assembly Checkpoint. *Cell Rep.* **14**, 1086–1099 (2016).
34. Ma, H. T. & Poon, R. Y. C. TRIP13 Functions in the establishment of the spindle assembly checkpoint by replenishing O-MAD2. *Cell Rep.* **22**, 1439–1450 (2018).
35. Yost, S. et al. Biallelic TRIP13 mutations predispose to Wilms tumor and chromosome missegregation. *Nat. Genet.* **49**, 1148–1151 (2017).
36. Foster, S. A. & Morgan, D. O. The APC/C Subunit Mnd2/Apc15 promotes Cdc20 autoubiquitination and spindle assembly checkpoint inactivation. *Mol. Cell* **47**, 921–932 (2012).
37. Mansfeld, J., Collin, P., Collins, M. O., Choudhary, J. S. & Pines, J. APC15 drives the turnover of MCC-CDC20 to make the spindle assembly checkpoint responsive to kinetochore attachment. *Nat. Cell Biol.* **13**, 1234–1243 (2011).
38. Uzunova, K. et al. APC15 mediates CDC20 autoubiquitylation by APC/C MCC and disassembly of the mitotic checkpoint complex. *Nat. Struct. Mol. Biol.* **19**, 1116–1123 (2012).
39. Ghandi, M. et al. Next-generation characterization of the Cancer Cell Line Encyclopedia. *Nature* **569**, 503–508 (2019).
40. Gaitanos, T. N. et al. Stable kinetochore-microtubule interactions depend on the Ska complex and its new component Ska3/C13Orf3. *EMBO J.* **28**, 1442–1452 (2009).
41. Hanisch, A., Silljé, H. H. W. & Nigg, E. A. Timely anaphase onset requires a novel spindle and kinetochore complex comprising Ska1 and Ska2. *EMBO J.* **25**, 5504–5515 (2006).
42. Raaijmakers, J. A., Tanenbaum, M. E., Maia, A. F. & Medema, R. H. RAMA1 is a novel kinetochore protein involved in kinetochore-microtubule attachment. *J. Cell Sci.* **122**, 2436–2445 (2009).
43. Theis, M. et al. Comparative profiling identifies C13orf3 as a component of the Ska complex required for mammalian cell division. *EMBO J.* **28**, 1453–1465 (2009).
44. Welburn, J. P. I. et al. The human kinetochore Ska1 complex facilitates microtubule depolymerization-coupled motility. *Dev. Cell* **16**, 374–385 (2009).
45. Zhang, G. et al. The Ndc80 internal loop is required for recruitment of the Ska complex to establish end-on microtubule attachment to kinetochores. *J. Cell Sci.* **125**, 3243–3253 (2012).
46. Schmidt, J. C. et al. The kinetochore-bound Ska1 complex tracks depolymerizing microtubules and binds to curved protofilaments. *Dev. Cell* **23**, 968–980 (2012).
47. Abad, M. A. et al. Ska3 Ensures timely mitotic progression by interacting directly with microtubules and Ska1 microtubule binding domain. *Sci. Rep.* **6**, 34042 (2016).
48. Cheerambathur, D. K. et al. Dephosphorylation of the Ndc80 tail stabilizes kinetochore-microtubule attachments via the Ska complex. *Dev. Cell* **41**, 424–437 (2017).
49. Monda, J. K. et al. Microtubule tip tracking by the spindle and kinetochore protein Ska1 requires diverse tubulin-interacting surfaces. *Curr. Biol.* **27**, 3666–3675 (2017).
50. Polley, S. et al. Stable kinetochore-microtubule attachment requires loop-dependent Ndc80-Ndc80 binding. *EMBO J.* **42**, https://doi.org/10.15252/embj.2022112504 (2023).
51. Maciejowski, J. et al. Mps1 Regulates kinetochore-microtubule attachment stability via the Ska complex to ensure error-free chromosome segregation. *Dev. Cell* **41**, 143–156.e6 (2017).
52. Auckland, P., Clarke, N. I., Royle, S. J. & McAinsh, A. D. Congressing kinetochores progressively load Ska complexes to prevent force-dependent detachment. *J. Cell Biol.* **216**, 1623–1639 (2017).
53. Huis In't Veld, P. J., Volkov, V. A., Stender, I. D., Musacchio, A. & Dogterom, M. Molecular determinants of the Ska-Ndc80 interaction and their influence on microtubule tracking and force-coupling. *Elife* **8**, https://doi.org/10.7554/eLife.49539 (2019).
54. Sivakumar, S. et al. The human SKA complex drives the metaphase-anaphase cell cycle transition by recruiting protein phosphatase 1 to kinetochores. *Elife* **5**, https://doi.org/10.7554/elife.12902 (2016).
55. Santaguida, S., Tighe, A., D'Alise, A. M., Taylor, S. S. & Musacchio, A. Dissecting the role of MPS1 in chromosome biorientation and the spindle checkpoint through the small molecule inhibitor reversine. *J. Cell Biol.* **190**, 73–87 (2010).
56. Daum, J. R. et al. Ska3 Is required for spindle checkpoint silencing and the maintenance of chromosome cohesion in mitosis. *Curr. Biol.* **19**, 1467–1472 (2009).
57. Sivakumar, S., Daum, J. R., Tipton, A. R., Rankin, S. & Gorbsky, G. J. The spindle and kinetochore-associated (Ska) complex enhances binding of the anaphase-promoting complex/cyclosome (APC/C) to chromosomes and promotes mitotic exit. *Mol. Biol. Cell* **25**, 594–605 (2014).
58. Belmontes, B. et al. Abstract 516: Discovery and preclinical characterization of AMG 650, a first-in-class inhibitor of kinesin KIF18A motor protein with potent activity against chromosomally unstable cancers. *Cancer Res.* **83**, 516–516 (2023).
59. Goshima, G., Mayer, M., Zhang, N., Stuurman, N. & Vale, R. D. Augmin: A protein complex required for centrosome-independent

microtubule generation within the spindle. *J. Cell Biol.* **181**, 421–429 (2008).
60. Goshima, G. et al. Genes required for mitotic spindle assembly in Drosophila S2 cells. *Science* **316**, 1249–1250 (2007).
61. Lawo, S. et al. HAUS, the 8-Subunit humanaugmin complex, regulates centrosome and spindle integrity. *Curr. Biol.* **19**, 816–826 (2009).
62. Petry, S., Pugieux, C., Nédélec, F. J. & Vale, R. D. Augmin promotes meiotic spindle formation and bipolarity in Xenopus egg extracts. *Proc. Natl. Acad. Sci. USA* **108**, 14473–14478 (2011).
63. Petry, S., Groen, A. C., Ishihara, K., Mitchison, T. J. & Vale, R. D. Branching microtubule nucleation in xenopus egg extracts mediated by augmin and TPX2. *Cell* **152**, 768–777 (2013).
64. Štimac, V., Koprivec, I., Manenica, M., Simunić, J. & Tolić, I. M. Augmin prevents merotelic attachments by promoting proper arrangement of bridging and kinetochore fibers. *Elife* **11**, https://doi.org/10.7554/eLife.83287 (2022).
65. Uehara, R. et al. The augmin complex plays a critical role in spindle microtubule generation for mitotic progression and cytokinesis in human cells. *PNAS* **106**, 6998–7003 (2009).
66. Zhu, H., Coppinger, J. A., Jang, C. Y., Yates, J. R. & Fang, G. FAM29A promotes microtubule amplification via recruitment of the NEDD1-γ-tubulin complex to the mitotic spindle. *J. Cell Biol.* **183**, 835–848 (2008).
67. Maerki, S. et al. The Cul3-KLHL21 E3 ubiquitin ligase targets Aurora B to midzone microtubules in anaphase and is required for cytokinesis. *J. Cell Biol.* **187**, 791–800 (2009).
68. Silver, D. L. et al. The exon junction complex component Magoh controls brain size by regulating neural stem cell division. *Nat. Neurosci.* **13**, 551–558 (2010).
69. Fukumura, K. et al. The exon junction complex controls the efficient and faithful splicing of a subset of transcripts involved in mitotic cell-cycle progression. *Int. J. Mol. Sci.* **17**, https://doi.org/10.3390/ijms17081153 (2016).
70. Fulcher, L. J. et al. FAM 83D directs protein kinase CK 1α to the mitotic spindle for proper spindle positioning. *EMBO Rep.* **20**, https://doi.org/10.15252/embr.201847495 (2019).
71. Matsumura, F., Yamakita, Y. & Yamashiro, S. Myosin light chain kinases and phosphatase in mitosis and cytokinesis. *Arch. Biochem. Biophys.* **510**, 76–82 (2011).
72. Yamashiro, S. et al. Myosin phosphatase-targeting subunit 1 regulates mitosis by antagonizing polo-like kinase 1. *Dev. Cell* **14**, 787–797 (2008).
73. Beck, J. et al. Ubiquitylation-dependent localization of PLK1 in mitosis. *Nat. Cell Biol.* **15**, 430–439 (2013).
74. Payton, M. et al. Small-molecule inhibition of kinesin KIF18A reveals a mitotic vulnerability enriched in chromosomally unstable cancers. *Nat. Cancer* https://doi.org/10.1038/s43018-023-00699-5 (2023).
75. Santaguida, S. et al. Chromosome Mis-segregation generates cell-cycle-arrested cells with complex karyotypes that are eliminated by the immune system. *Dev. Cell* **41**, 638–651 (2017).
76. Mayr, M. I. et al. The human kinesin Kif18A is a motile microtubule depolymerase essential for chromosome congression. *Curr. Biol.* **17**, 488–498 (2007).
77. Stumpff, J., von Dassow, G., Wagenbach, M., Asbury, C. & Wordeman, L. The kinesin-8 motor Kif18A suppresses kinetochore movements to control mitotic chromosome alignment. *Dev. Cell* **14**, 252–262 (2008).
78. Zeng, X. et al. Pharmacologic inhibition of the anaphase-promoting complex induces a spindle checkpoint-dependent mitotic arrest in the absence of spindle damage. *Cancer Cell* **18**, 382–395 (2010).
79. Klaasen, S. J. et al. Mitotic adaptations shape acquired resistance and vulnerabilities to KIF18A inhibition in cancer.https://doi.org/10.64898/2026.08.07.743460 (2026).
80. Vasan, N., Baselga, J. & Hyman, D. M. A view on drug resistance in cancer. *Nature* **575**, 299–309 (2019).
81. Andreu, C. et al. KIF18A Inhibition as a therapeutic strategy in cancers with Rb pathway inactivation.http://biorxiv.org/lookup/doi/10.64898/2026.04.14.718587 (2026).
82. Ashworth, A. & Lord, C. J. Synthetic lethal therapies for cancer: what's next after PARP inhibitors? *Nat. Rev. Clin. Oncol.* **15**, 564–576 (2018).
83. Sdeor, E., Okada, H., Saad, R., Ben-Yishay, T. & Ben-David, U. Aneuploidy as a driver of human cancer. *Nat. Genet.* **56**, 2014–2026 (2024).
84. Hinterndorfer, M., Spiteri, V. A., Ciulli, A. & Winter, G. E. Targeted protein degradation for cancer therapy. *Nat. Rev. Cancer* **25**, 493–516 (2025).
85. van der Weegen, Y. et al. ELOF1 is a transcription-coupled DNA repair factor that directs RNA polymerase II ubiquitylation. *Nat. Cell Biol.* **23**, 595–607 (2021).
86. Brinkman, E. K., Chen, T., Amendola, M. & Van Steensel, B. Easy quantitative assessment of genome editing by sequence trace decomposition. *Nucleic Acids Res.* **42**, https://doi.org/10.1093/nar/gku936 (2014).
87. Hart, T. et al. Evaluation and design of genome-wide CRISPR/SpCas9 knockout screens. *G3* **7**, 2719–2727 (2017).
88. Colic, M. et al. Identifying chemogenetic interactions from CRISPR screens with drugZ. *Genome Med.* **11**, https://doi.org/10.1186/s13073-019-0665-3 (2019).
89. de Lint, K. IsogenicZ. *GitHub*https://github.com/kdelint/IsogenicZ.git (2023).
90. Aleksander, S. A. et al. The Gene Ontology knowledgebase in 2023. *Genetics* **224**, https://doi.org/10.1093/genetics/iyad031 (2023).
91. Ashburner, M. et al. Gene Ontology: Tool for the unification of biology. **25**, 25–29 (2000).
92. Snel, B., Lehmann, G., Bork, P. & Huynen, M. A. STRING: A web-server to retrieve and display the repeatedly occurring neighbourhood of a gene. *Nucleic Acids Res.* **28**,http://www.bork.embl-heidelberg.de/STRING (2000).
93. Szklarczyk, D. et al. The STRING database in 2023: protein-protein association networks and functional enrichment analyses for any sequenced genome of interest. *Nucleic Acids Res.* **51**, D638–D646 (2023).
94. Bissonette, S. & Stumpff, J. Quantifying mitotic chromosome dynamics and positioning. *J. Cell. Physiol.* **229**, 1301–1305 (2014).
95. Langmead, B. & Salzberg, S. L. Fast gapped-read alignment with Bowtie 2. *Nat. Methods* **9**, 357–359 (2012).
96. Jun, G., Wing, M. K., Abecasis, G. R. & Kang, H. M. An efficient and scalable analysis framework for variant extraction and refinement from population-scale DNA sequence data. *Genome Res.* **25**, 918–925 (2015).
97. Bakker, B. et al. Single-cell sequencing reveals karyotype heterogeneity in murine and human malignancies. *Genome Biol.* **17**, https://doi.org/10.1186/s13059-016-0971-7 (2016).
98. van den Bos, H. et al. Single-cell whole genome sequencing reveals no evidence for common aneuploidy in normal and Alzheimer's disease neurons. *Genome Biol.* **17**, https://doi.org/10.1186/s13059-016-0976-2 (2016).
99. Arafeh, R., Shibue, T., Dempster, J. M., Hahn, W. C. & Vazquez, F. The present and future of the Cancer Dependency Map. *Nat. Rev. Cancer* **25**, 59–73 (2025).
100. Zerbib, J. et al. Human aneuploid cells depend on the RAF/MEK/ERK pathway for overcoming increased DNA damage. *Nat. Commun.* **15**, 7772 (2024).

Acknowledgements
We thank Isabel Potters (Princess Máxima Center for pediatric oncology) for computational support, Iain Cheeseman (Whitehead Institute for Biomedical Research, Cambridge, USA), Geert Kops (Hubrecht Institute, Utrecht, The Netherlands), Marcel van Vugt (UMC Groningen, Groningen, The Netherlands), Stefano Santaguida (IEO, Milan, Italy) and Andrea Musacchio (Max Planck Institute of molecular physiology, Dortmund, Germany) for reagents, and Marialucrezia Losito (IPSomics) for scWGS analysis. We acknowledge Stefano Maffini (Max Planck Institute of Molecular Physiology) and Marco Novais-Cruz (Princess Máxima Center for Pediatric Oncology) for discussions. We thank members of the Medema-Vader lab for input and support, and Pim Huis in 't Veld (Max Perutz Labs, Vienna, Austria) for discussions and in silico protein complex modeling. We thank Martijn Luijsterburg and Sjoerd Klaasen (LUMC, Leiden, The Netherlands) for sharing unpublished observations and for Sovilnesib. We acknowledge Marcel van Vugt, Andreas Hochwagen (NYU, New York, USA) and Valentina Piano (University of Cologne, Cologne, Germany) for input on the manuscript.

Author contributions
Experimentation: M.S.U., E.S.C., K.V., D.R., K.d.L., M.A.R., and T.D.K. Conceptualization: M.S.U., G.V., U.B.D., and R.H.M. Data analysis and computation: M.S.U., K.d.L., A.T., and I.J.H. Supervision: G.V., U.B.D., R.M.F.W., R.D.L., I.M.T., and F.F. Project management: M.S.U., G.V., U.B.D., R.M.F.W., and R.D.L. Funding acquisition: G.V., R.H.M., I.M.T., U.B.D., R.M.F.W., and F.F. Writing: M.S.U. and G.V. with input from all authors.

Funding
G.V. discloses support for the research of this work from Amsterdam UMC (AUMC research fellowship) and the Dutch Cancer Society (KWF exploration grant 15228). RMFW discloses support for the research of this work from Amsterdam UMC (ADORE 2024-9-01). UBD discloses support for the research of this work from the European Research Council (Starting Grant 945674) and Israel Cancer Association (Grant 20230018). IMT discloses support for the research of this work from the Croatian Science Foundation (Grant IP-2024-05-5336), Croatian Science Foundation (Grant IPCH-2022-10-9344), European Research Council (Synergy Grant 855158), and Scientific Center of Excellence - QuantiXLie (Grant PK.1.1.10.0004). R.H.M. discloses support for the research of this work from Oncode Institute.

Competing interests
U.B.D. received consulting fees from Accent Therapeutics. F.F. is Chief Scientific Officer of iPsomics B.V. He does not stand financial benefits from this role. All other authors declare no competing interests.

Additional information
Supplementary information The online version contains supplementary material available at https://doi.org/10.1038/s41467-026-79311-0.

Correspondence and requests for materials should be addressed to Gerben Vader.

Peer review information *Nature Communications* thanks the anonymous reviewers for their contribution to the peer review of this work. A peer review file is available.

Reprints and permissions information is available at http://www.nature.com/reprints

Publisher's note Springer Nature remains neutral with regard to jurisdictional claims in published maps and institutional affiliations.

Open Access This article is licensed under a Creative Commons Attribution-NonCommercial-NoDerivatives 4.0 International License, which permits any non-commercial use, sharing, distribution and reproduction in any medium or format, as long as you give appropriate credit to the original author(s) and the source, provide a link to the Creative Commons licence, and indicate if you modified the licensed material. You do not have permission under this licence to share adapted material derived from this article or parts of it. The images or other third party material in this article are included in the article's Creative Commons licence, unless indicated otherwise in a credit line to the material. If material is not included in the article's Creative Commons licence and your intended use is not permitted by statutory regulation or exceeds the permitted use, you will need to obtain permission directly from the copyright holder. To view a copy of this licence, visit http://creativecommons.org/licenses/by-nc-nd/4.0/.

© The Author(s) 2026